NUMERICAL SIMULATION OF HYDRODYNAMIC PLANAR MOTION MECHANISM TEST FOR UNDERWATER VEHICLES

A THESIS SUBMITTED TO
THE GRADUATE SCHOOL OF NATURAL AND APPLIED SCIENCES
OF
MIDDLE EAST TECHNICAL UNIVERSITY

BY

MUSTAFA CAN

IN PARTIAL FULFILLMENT OF THE REQUIREMENTS
FOR
THE DEGREE OF MASTER OF SCIENCE
IN
AEROSPACE ENGINEERING

SEPTEMBER 2014

Approval of the thesis

NUMERICAL SIMULATION OF HYDRODYNAMIC PLANAR MOTION MECHANISM TEST FOR UNDERWATER VEHICLES

Submitted by **MUSTAFA CAN** in partial fulfillment of the requirements for the degree of **Master of Science in Aerospace Engineering Department, Middle East Technical University** by,

Prof. Dr. Canan Özgen ________________
Dean, Graduate School of **Natural and Applied Sciences**

Prof. Dr. Ozan Tekinalp ________________
Head of Department, **Aerospace Engineering**

Assoc. Prof. Dr. Sinan Eyi ________________
Supervisor, **Aerospace Engineering Dept., METU**

Examining Committee Members:

Prof. Dr. Nafiz Alemdaroğlu ________________
Aerospace Engineering Dept., METU

Assoc. Prof. Dr. Sinan Eyi ________________
Aerospace Engineering Dept., METU

Prof. Dr. İsmail Hakkı Tuncer ________________
Aerospace Engineering Dept., METU

Prof Dr. Serkan Özgen ________________
Aerospace Engineering Dept., METU

Bora Atak, M.Sc. ________________
Specialist Engineer, ROKETSAN

Date: 03/09/2014

I hereby declare that all the information in this document has been obtained and presented in accordance with academic rules and ethical conduct. I also declare that, as required by these rules and conduct, I have fully cited and referenced all material and results that are not original to this work.

Name, Last name : Mustafa CAN

Signature :

ABSTRACT

NUMERICAL SIMULATION OF HYDRODYNAMIC PLANAR MOTION MECHANISM TEST FOR UNDERWATER VEHICLES

Can, Mustafa
M.S., Department of Aerospace Engineering
Supervisor: Assoc. Prof. Dr. Sinan Eyi

September 2014, 97 Pages

Several captive tests, such as; PMM (Planar Motion Mechanism), RA (Rotating Arm), straight-line towing tests and CMM (Coning Motion Mechanism) can be conducted to obtain hydrodynamic coefficients or maneuvering derivatives that are necessary for system simulation of AUVs (Autonomous Underwater Vehicles). Development of computer technology provides an opportunity to solve flow problems by using CFD (Computational Fluid Dynamics). Therefore modeling hydrodynamic tests by using CFD methods is another option to obtain hydrodynamic coefficients. In this thesis, CFD modelling techniques are developed to simulate towing tests, rotating arm tests and planar motion mechanism tests. These test scenarios are modeled by using CFD methods. Commercial flow solver FLUENT is used to solve these flow problems. Straight-line towing tests are simulated for DARPA (Defense Advanced Research Projects Agency) and UK Natural Environment Research Council's Autosub test-case models. Rotating arm and planar motion mechanism tests are simulated for Autosub test-case model. Rotating arm tests are simulated for constant angular velocity and constant angular acceleration. Then two different motions are simulated in the scope of PMM studies. FLUENT user defined functions are used for analyses that mesh motions are needed. Analyses results are compared with experimental data available in literature.

Keywords: Computational Fluid Dynamics, Hydrodynamic Coefficients, DARPA, Autosub, Planar Motion Mechanism, Rotating Arm, Towing Test, Autonomous Underwater Vehicle.

ÖZ

SU ALTI ARAÇLARI İÇİN DÜZLEMSEL HAREKET MEKANİZMASI TESTİNİN SAYISAL OLARAK MODELLENMESİ

Can, Mustafa
Yüksek Lisans, Havacılık ve Uzay Mühendisliği Bölümü
Tez Yöneticisi: Assoc. Prof. Dr. Sinan Eyi

Eylül 2014, 97 Sayfa

Otonom su altı araçlarının sistem benzetimi için gerekli olan hidrodinamik katsayıları veya manevra türevlerini elde etmek için düzlemsel hareket, döner kol, çekme ve konileme hareketi gibi çeşitli testler gerçekleştirilir. Bilgisayar teknolojisinin gelişmesi ile Hesaplama Akışkanlar Dinamiği (HAD) yöntemleri akış problemlerinin çözümü için sıkça kullanılmaktadır. Bu sebeple hidrodinamik testlerinin hesaplamalı akışkanlar mekaniği yöntemleri kullanılarak modellenmesi, hidrodinamik katsayıların hesaplanması için farklı bir seçenek haline gelmiştir. Bu tez çalışmasında, çekme testi, döner kol testi ve düzlemsel hareket testi için hesaplamalı akışkanlar mekaniği modelleme teknikleri geliştirilmiştir. Bu test senaryoları HAD yöntemleri kullanılarak modellenmiştir. FLUENT ticari akış çözücü programı, bu akış problemlerini çözmek için kullanılmıştır. Statik Çekme testleri için DARPA ve Autosub denek-taşı modelleri kullanılmıştır. Döner kol ve düzlemsel hareket analizleri için Autosub denek-taşı modeli kullanılmıştır. Döner kol testi benzetimi sabit açısal hızlı ve sabit açısal ivmeli hareketler için gerçekleştirilmiştir. Düzlemsel hareket çalışmaları kapsamında ise iki farklı hareket HAD yöntemleri kullanılarak modellenmiştir. FLUENT kullanıcı tanımlı fonksiyonları çözüm ağı hareketine ihtiyaç duyulan analizler için kullanılmıştır. Analiz sonuçları literatürde yer alan deneysel veriler ile kıyaslanmıştır.

Anahtar Kelimeler: Hesaplamalı Akışkanlar Dinamiği, Hidrodinamik Katsayılar, DARPA, Autosub, Düzlemsel Hareket Mekanizması, Döner Kol, Sualtı Çekme Testi, İnsansız Sualtı Aracı.

To My Family

ACKNOWLEDGEMENTS

I wish my deepest gratitude to my supervisor Prof. Dr. Sinan Eyi for his guidance, advice, criticism and encouragements throughout the thesis.

I also wish to thank my department manager Mr. Ali Akgül for his guidance and support during this study. I also would like to thank my colleagues in Aerodynamics Department of ROKETSAN for all their help and support during the thesis.

I am very thankful to my parents Mrs. Sahadet Can, Mr. Abdullah Can and my brother Mr. Hakan Can for their help and motivation. Without them this work would not be completed.

I want to express my best wishes to Mr. Iskender Kayabaşı, Mr. Tolga Aydoğdu and Mr. Emrah Gülay for their friendship and support during this study.

TABLE OF CONTENTS

CHAPTERS

LIST OF FIGURES

FIGURES

LIST OF TABLES

TABLES

LIST OF SYMBOLS

AUV	Autonomous Underwater Vehicle
UV	Underwater Vehicle
RA	Rotating Arm
PMM	Planar Motion Mechanism
CMM	Coning Motion Mechanism
CFD	Computational Fluid Dynamics
BC	Boundary Condition
AOA	Angle of Attack
UDF	User Defined Function
R	Radius of Rotating Arm
L	Length of Test-case Model
V	Free-stream Velocity
a	Amplitude of Sinusoidal Function
f	Frequency of Sinusoidal Function
t	Time
X'	X Force Coefficient
Z'	Z Force Coefficient
M'	Pitch Moment Coefficient
Z'_q	Z Force Coefficient Derivative with Pitch Rate
M'_q	Pitch Moment Coefficient Derivative with Pitch Rate
Z'_w	Z Force Coefficient Derivative with Z Velocity
M'_w	Pitch Moment Coefficient Derivative with Z Velocity

$Z'_{\dot{q}}$	Z Force Coefficient Derivative with Pitch Acceleration
$M'_{\dot{q}}$	Pitch Moment Coeff. Derivative with Pitch Acceleration
$Z'_{\dot{w}}$	Z Force Coefficient Derivative with Z Acceleration
$M'_{\dot{w}}$	Pitch Moment Coefficient Derivative with Z Acceleration
w'	Non-Dimensional Z velocity
$\dot{w}'$	Non-Dimensional Z acceleration
q'	Non-Dimensional Pitch Rate
$\dot{q}'$	Non-Dimensional Pitch Acceleration

CHAPTER 1

INTRODUCTION

In recent years, developments in technology provide opportunities to use unmanned vehicles for different purposes. In this way, unmanned vehicles remove risks for human life and can accomplish risky tasks which human body cannot handle. All of the unmanned vehicles have technical requirements and design goals according to purposes of use. Especially, autonomous unmanned vehicles that are controlled by an autopilot in accordance with a significant course must be designed in detail. Main steps of design process must be well built and examined to reach the correct design. Hydrodynamic design and analysis studies lead steps of an autonomous underwater vehicle design process. Hydrodynamics is classified under fluid dynamics science and hydrodynamics deals with incompressible flows. In general, hydrodynamics deals with fluids resistance on objects sunken into fluid, causes of occurrence of resistance, characteristics of fluid and fluid motions. Hydrodynamic effects must be considered for effective usage of underwater world. Within this scope, AUVs are one type of important vehicles that are used for underwater researches. Works on use of AUVs become more important day by day. AUVs can be used for different purposes such as; military, commercial and scientific purposes but AUVs can have different design and performance parameters according to usage purpose [1]. Hydrodynamic design and analyses of AUVs must be done well for successful task results.

1.1 General Information about Autonomous Underwater Vehicles

There are various underwater vehicles that are used in different applications. Underwater vehicles can be classified under several groups in accordance with their specifications. Figure 1.1 shows classification of UVs according to control method of underwater vehicles.

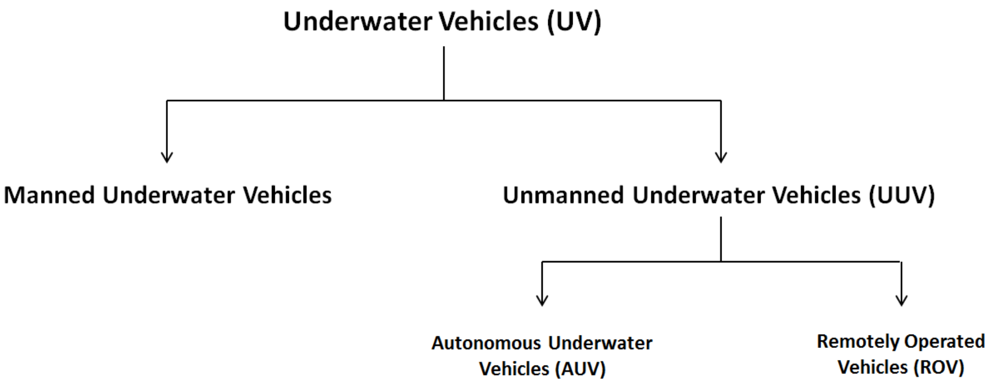

Figure 1.1 Classification of Underwater Vehicles by Control Method [2]

AUVs are hydrodynamic form shaped robotic vehicles which have abilities to be programmed for different missions and to cruise in various underwater conditions without any human or remote human control [3]. AUVs can receive signals from a satellite to reach desired coordinates. Some of AUVs process data from their acoustic sensors to guide themselves autonomously. Figure 1.2 shows Autosub AUV.

Figure 1.2 Autosub AUV [4]

As mentioned before, AUVs can be used for scientific, commercial and military purposes. AUVs can work at high pressures that human body cannot resist. In addition AUVs have modular structure. Through this specification different sub-parts can be integrated to AUV and AUV can be used for different purposes. Thus it can be said that modular structure of AUVs increases efficiency and decrease operation costs.

1.2 Hydrodynamic Design and Analysis

Hydrodynamic database are most important input data for system simulation of an AUV. Numerical, semi-empirical and experimental methods can be used to generate hydrodynamic database for an AUV. It is certain that experimental methods are most reliable methods to generate a hydrodynamic database but conducting an experiment is much more expensive compared to other methods. However numerical and semi-empirical methods can be an alternative to generate hydrodynamic database during pre-design or conceptual design processes of an AUV. In this way, number and costs of hydrodynamic tests can be reduced. In this study, CFD modelling techniques are developed as a numerical solution to simulate several hydrodynamic tests.

1.2.1 Numerical Methods

Numerical methods include analytical and CFD methods. Analytical methods are applicable for simplified problems and cannot be used for complex equations. However CFD methods become very helpful tools for an AUV design processes with through the development of computer technology. Generally, CFD methods are used to simulate hydrodynamic tests to predict hydrodynamic characteristics of the model. In addition CFD modelling techniques are changed according to hydrodynamic test including different motions. Therefore accuracy and computational time varies according to used CFD modelling techniques.

1.2.2 Semi-empirical Methods

Semi-empirical methods include simplified theories and empirical corrections derived from experimental data. There are semi-empirical fast prediction codes that use experimental database and component build up method to predict aerodynamic or hydrodynamic characteristic of a model. However developed fast prediction codes for hydrodynamic problems, are not open source and reliable. In addition these codes are expensive.

1.2.3 Experimental Methods

In this study, straight-line towing, RA and PMM tests are simulated by using CFD methods. Brief information about these tests is given below:

1.2.3.1 Straight-Line Towing Test

Towing tests are conducted to obtain static coefficients. Scaled or non-scaled model is connected and fastened to the arms of mechanism. Desired angle of attack or yaw angle or roll angle can be adjusted before fastening. Also control surfaces can be deflected and static hydrodynamic coefficients can be calculated for this configuration too. Figure 1.3 shows a sample arrangement for straight line towing test [5].

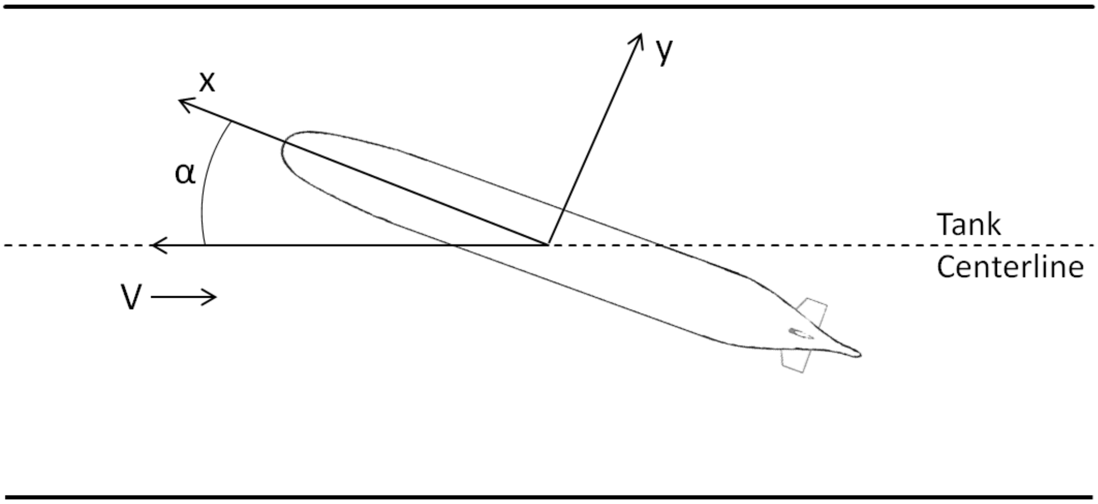

Figure 1.3 Straight Line Towing Test Arrangement [6]

Angular or time dependent velocities cannot be defined for straight line towing test mechanisms. Therefore model is towed with constant speed in the towing tank. Hydrodynamic forces and moments that act on the model can be measured at 3 different axes. A towing tank has been shown in Figure 1.4.

Figure 1.4 Towing Tank [5]

Measured values include forces and moments acting on the arms of the mechanisms. Therefore arms are towed alone in the towing tank to calculate force and moment values on the model. Measured hydrodynamic forces and moments are non-dimensionalized by desired values to the obtain hydrodynamic coefficients [7].

1.2.3.2 Rotating Arm Test

Rotating arm test is similar to straight line test, but model is towed in a circular path. Turning radius can be adjusted to desired length within limits of RA [6]. Linear velocity of model can be varied by changing turning radius or angular velocity. RA test mechanism arrangement has been shown in Figure 1.5.

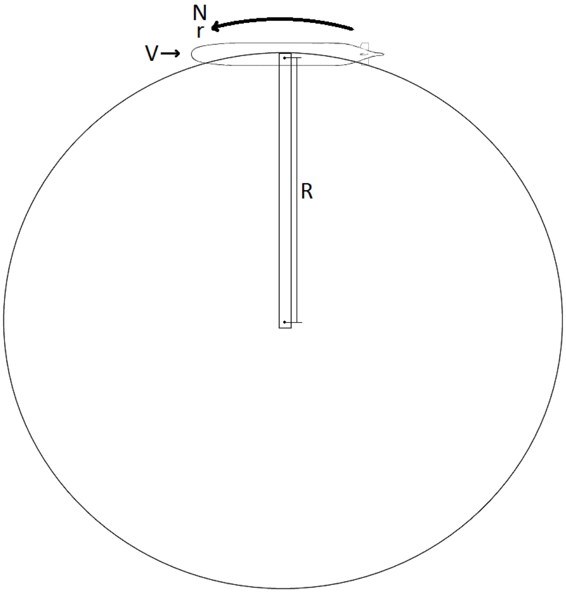

Figure 1.5 Rotating Arm Test Arrangement [6]

RA tests need larger towing tank compared to straight line towing tests as a result of circular path. Figure 1.6 shows an instance for RA towing tank.

Figure 1.6 Rotating Arm Towing tank

RA tests can be conducted on yaw plane and pitch plane. Generally, RA tests are conducted to obtain non-linear dynamic derivatives (pitch rate dependent or yaw rate dependent derivatives).

1.2.3.1 Planar Motion Mechanism Test

PMM is the most comprehensive test among hydrodynamic tests. Models are towed with constant speed in both straight-line towing and RA tests so that acceleration dependent hydrodynamic derivatives cannot be obtained [6]. However velocity dependent derivatives, rotary dependent derivatives and acceleration dependent derivatives (also known as added mass or added inertia derivatives) can be obtained by conducting a PMM test with oscillatory motion. PMM consists of a carriage and two force transducers (forward and aft force transducers). Carriage tows model with a constant speed in the tank. One of the force transducers produces transverse oscillation at the front of the model and the other one produces transverse oscillation at the aft of the model [8]. PMM test arrangement has been shown in Figure 1.7.

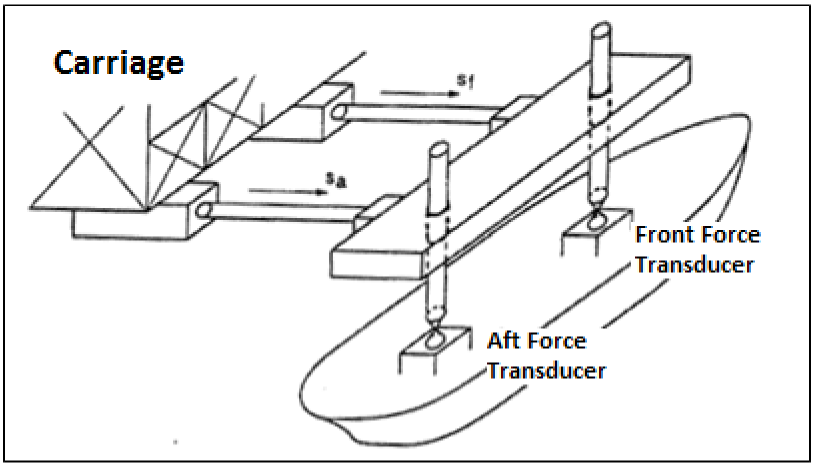

Figure 1.7 PMM Test Arrangement [6]

Model can be forced to do oscillatory motions in the towing tank such as pure yaw, pure sway and combination of these two motions on horizontal plane. In addition, pure sway and pure yaw motions are named as pure heave and pure pitch on vertical plane. Oscillator motion modes of PMM can be seen in Figure 1.8.

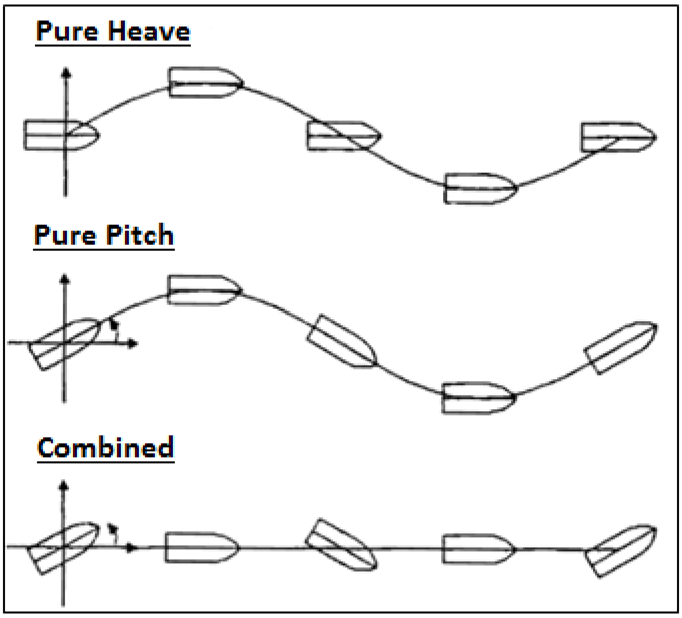

Figure 1.8 PMM Oscillatory Motion Modes on Vertical Plane [9]

Similar to the straight-line towing tests PMM needs longer and narrower towing tank to perform these oscillatory motion modes. Figure 1.9 shows PMM and towing tank during an AUV model test.

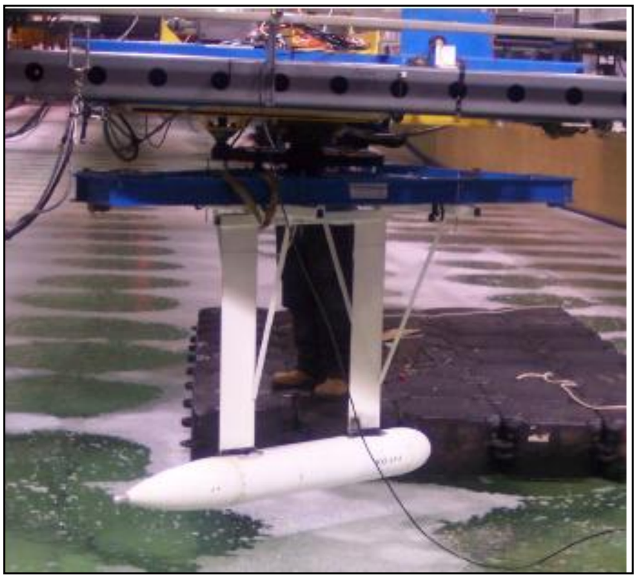

Figure 1.9 PMM and Towing Tank during an AUV Test [10]

1.3 Literature Survey

Previous studies mostly were done to define maneuverability or stability characteristics of UVs. In other words studies were performed to obtain hydrodynamic coefficients. There are plenty of studies based on experiments and analytical, empirical and CFD methods. However most of the earlier studies do not include CFD methods due to the lack of computer technologies.

David and Jackson [11] used a coning motion apparatus for a hydrodynamic test first time in history. They intended to investigate non-planar cross flow effects especially on yaw and roll derivatives. Then this test apparatus is used commonly and it earned a well-known name which is coning motion mechanism. Roddy [12] conducted captive-model experiments for several DARPA SUBOFF model configurations to investigate different configurations' hydrodynamic stability and control characteristics. He stated that model was unstable in all of the test conditions. Kimber and Scrimshaw [13] conducted PMM and RA tests for ¾ scale Autosub model to determine hydrodynamic characteristics of the vehicle and to calculate appropriate size and geometry of control surfaces. Guo and Chiu [14] conducted hydrodynamic tests on horizontal and vertical model of AUV-HM1. Then they used experimental data to develop a prediction method for maneuverability of a flat-streamlined UV.

Humphreys and Watkinson [15] used analytical methods to estimate hydrodynamic coefficients for UVs from their geometric parameters. Calculated acceleration derivatives of UV were compared with experimental data. It was stated that only four of fifteen calculated coefficients have error percentage above %12. Jones et al. [16] used analytical and semi-empirical methods to calculate hydrodynamics derivatives of AUVs according to their shapes and sizes. They used U.S. Datcom method, Roskam method and The University of London Method which are applicable to standard aeroplane configurations. Applications were made for MARK 13, MARK 18, MARK 36 and MARK 41 torpedoes. Calculation results were compared with experimental data. It was concluded that because of the differences between AUVs and aeroplane shapes, none of the methods provides necessary accuracy for calculations. Barros et al. [17] studied the usage of analytical and semi-empirical methods to estimate hydrodynamic derivatives of most popular class of AUVs. An implementation has been carried out to estimate hydrodynamic derivatives of MAYA AUV which is being developed by corporation of Indian-Portuguese.

Philips et al. [4] used CFD methods to simulate hydrodynamic towing test and rotating arm test for Autosub model. Besides they used SST k-ω and k-ε turbulence models for CFD analyses. They showed that force and moment coefficients obtained from analyses results were close enough to experimental data for both of the turbulence models. However results of k-ε turbulence model were slightly more accurate than the k-ω results. In addition it was indicated that estimated dynamic stability margin of Autosub was very consistent with experimental value. Moreover Philips et al. [18] have developed a robust CFD method to simulate PMM test. Pure sway motion is simulated for Autosub AUV model. They used multi-block structured mesh to simplify flow domain and to reduce computational time. Calculated yaw force and yaw moment coefficients were compared with experimental data. It was expressed that error percentages of coefficients was below %26. Zang et al. [19] have developed a modelling technique to simulate hydrodynamic tests by using CFD software FLUENT. Long endurance underwater vehicle (LEUV) model was used for analyses. Calculated coefficients were used for system simulation of LEUV. They stated that developed CFD methods could satisfy the need of establishing system simulation to predict maneuverability of an AUV during design process. Kim et al. [20] used CFD methods to simulate turning maneuver of DARPA SUBOFF body. They intended to investigate turbulent flow around the body. Two different turbulence models; The Wilcox' k-ω and SST k-ω have been used for CFD analyses. Because of the model was moved by a sting during experiments, analyses were performed for model with sting and without sting. Analyses results were compared with experimental data. They indicated that Wilcox' k-ω turbulence model is better than SST k-ω turbulence model in capturing vortices and other features of the flow. Also it was stated that the sting has low but evaluable effects on the flow and forces acting on the body. Arslan [21] developed CFD modelling techniques to predict a

AUVs’ hydrodynamic characteristics. He simulated towing and rotating arm tests for Autosub AUV model by using CFD methods and calculated dynamic and static hydrodynamic coefficients. Analyses results were compared with experimental data to validate methods. Calculated coefficients were used for system simulation of Autosub.

1.4 Aim of the Thesis

Most reliable way to determine hydrodynamic characteristics of an AUV is conducting hydrodynamic tests. Therefore hydrodynamic tests are inevitable parts of an AUV design process. On the other hand development of computer technologies provides opportunities to simulate hydrodynamic tests by using CFD methods. Related studies about CFD modelling of hydrodynamic tests are given in previous section. CFD methods are used as an assistive tool for AUV design processes. However development of CFD modelling techniques increases usage of CFD methods during design processes. In this way hydrodynamic test requirements and costs of an AUV design projects can be reduced. This study aims to help development of CFD modelling techniques to simulate hydrodynamic tests such as straight line towing, RA and PMM tests.

CHAPTER 2

FLOW SOLVER METHODOLOGY

In this study FLUENT commercial code is used as flow solver. Incompressible fluid flow, compressible fluid flow, heat transfer, finite rate chemistry, species transport, combustion, multiphase flow, solidification and melting problems can be solved as steady-state or time dependently by FLUENT. A wide variety of different mesh types for both 2D and 3D flow domains can be imported FLUENT [22]. Methodology of flow solver for used features will be given in this chapter.

2.1 Governing Equations

FLUENT solves mass and momentum conservation equations for all flow problems. If problem include compressibility or heat transfer, conservation of energy equation is added to equation system [23]. In this study fluid is water so that it is assumed that flow is incompressible and there is no heat transfer. Conservation equations of mass and momentum are given below.

2.1.1 Conservation of Mass

Conservation of mass equation is also known as continuity equation. It can be written as follows:

$$\frac{\partial \rho}{\partial t} + \nabla \cdot (\rho \vec{v}) = S_m \tag{2.1}$$

In the equation, ρ is the density, t is the time, $\vec{v}$ is the velocity vector and S_m is the source term. This equation general form of the conservation of mass equation and it is valid for both incompressible and compressible flows. If problem is not time-dependent, t derivatives equal to zero and if fluid is incompressible, ρ changes equal to zero.

2.1.2 Conservation of Momentum

Conservation of momentum equation is given as follows [24].

$$\frac{\partial}{\partial t}(\rho\vec{v}) + \nabla \cdot (\rho\vec{v}\vec{v}) = -\nabla p + \nabla \cdot (\bar{\bar{\tau}}) + \rho\vec{g} + \vec{F} \tag{2.2}$$

Where p is the static pressure, $\bar{\bar{\tau}}$ is the stress tensor and $\rho\vec{g}$ and $\vec{F}$ are the gravitational and external body forces. $\vec{F}$ also covers other source terms. The stress tensor $\bar{\bar{\tau}}$ is described with equation 2.3.

$$\bar{\bar{\tau}} = \mu\left[(\nabla\vec{v} + \nabla\vec{v}^T) - \frac{2}{3}\nabla \cdot \vec{v}I\right] \tag{2.3}$$

Molecular viscosity is represented by μ and I indicates the unit tensor.

2.2 Turbulence Modelling

In this part, theoretical background of turbulence modelling are given.

2.2.1 Reynolds Averaged Navier-Stokes

Reynolds averaging method decompound solution variables in the Navier-Stokes equations into the mean and fluctuating components. Velocity components are written in Reynolds Averaging as follows [23]:

$$u_i = \bar{u}_i + u_i' \tag{2.4}$$

Where $\bar{u}_i$ term is the mean component and u_i' term is the fluctuating component of velocity (i= 1, 2, 3...)

This decomposing method can applied other scalar quantities:

$$\emptyset_i = \bar{\emptyset}_i + \emptyset_i' \tag{2.5}$$

Where $\emptyset$ express a scalar quantity such as energy, pressure etc.

Reynolds averaged continuity and momentum equations can be written in Cartesian tensor form by substituting decomposed form of flow variables into the continuity and momentum equations and taking time average:

$$\frac{\partial \rho}{\partial t} + \frac{d}{dx}(\rho u_i) = 0 \tag{2.6}$$

$$\frac{d}{dt}(\rho u_i) + \frac{d}{dx_j}\left(\rho u_i u_j\right) = -\frac{dp}{dx_i} + \frac{d}{dx_j}\left[\mu\left(\frac{du_i}{dx_j} + \frac{du_j}{dx_i} - \frac{2}{3}\delta_{ij}\frac{du_l}{dx_l}\right)\right] + \frac{d}{dx_j}\left(-\rho\overline{u_i' u_j'}\right) \tag{2.7}$$

Equations (2.6) and (2.7) are called as Reynolds Averaged Navier-Stokes Equations. There are additional terms in Reynolds averaged form of momentum equation. These terms represents effects of turbulence and called as Reynolds stresses. The Reynolds stresses $(-\rho\overline{u_i' u_j'})$ must be modelled to simplify Equation (2.7) [23].

2.2.2 Boussinesq Approach and Reynolds Stress Transport Models

Modelling of Reynolds stresses are required to model turbulence by using Reynolds-averaged approach. Boussinesq hypothesis is a commonly used approach to write Reynolds stresses in terms of mean velocity gradients. Reynolds stresses can be written as follows according to Boussinesq approach [25]:

$$\left(-\rho\overline{u_i' u_j'}\right) = \mu_t\left(\frac{du_i}{dx_j} + \frac{du_j}{dx_i}\right) - \frac{2}{3}\left(\rho k + \mu_k\frac{du_k}{dx_k}\right)\delta_{ij} \tag{2.8}$$

The Boussinesq Approach is used in Sparat-Allmaras, k-ε and k-ω turbulence models. This method requires low computational effort for computation of the turbulent viscosity. In Sparat-Allmaras model, one additional transport equation is solved and two additional transport equations are solved in k-ε and k-ω turbulence models. Turbulent viscosity is related with turbulent kinetic energy (k), turbulent dissipation rate (ε) or specific dissipation rate (ω). However Boussinesq hypothesis assumes that turbulent viscosity is an isotropic scalar quantity. This assumption does not cover all flow problems but it works well for shear flows which are dominated by only one of the shear stresses such as mixing layers, boundary layers and jets [23].

2.2.3 Turbulence Models

In this study Sparat-Allmaras, Reliable k-ε and SST k-ω turbulence models are used for at least one flow problem. General information about theory of these turbulence models will be given in this part.

2.2.3.1 Sparat-Allmaras Turbulence Model

Sparat-Allmaras is a one equation turbulence model. Modelled transport equation is solved for kinematic turbulent viscosity. The Sparat-Allmaras turbulence model was originally developed for aerospace applications especially wall-bounded flows and boundary layers that are sustained to adverse pressure gradients. Hence, it is not appropriate for all flow problems and causes larger errors for free shear flows such as round and plane jet flows. In addition, the Sparat-Allmaras turbulence model is not trustworthy for predicting decay of isotropic and homogeneous turbulence [23].

Sparat-Allmaras transport equation is modelled for $\tilde{\nu}$ which is identical to turbulent kinematic viscosity except in the near-wall region. It is given as follows:

$$\frac{\partial}{\partial t}(\rho\tilde{\nu}) + \frac{\partial}{\partial x_i}(\rho\tilde{\nu}u_i) = G_\nu - Y_\nu + S_{\tilde{\nu}} + \frac{1}{\sigma_{\tilde{\nu}}}\left[\frac{\partial}{\partial x_j}\left\{(\mu + \rho\tilde{\nu})\frac{\partial\tilde{\nu}}{\partial x_j}\right\} + C_{b2}\rho\left(\frac{\partial\tilde{\nu}}{\partial x_j}\right)^2\right] \tag{2.9}$$

Where ν is the kinematic viscosity, $S_{\tilde{\nu}}$ is the source term and $\sigma_{\tilde{\nu}}$ and C_{b2} are constants. Generation of turbulent viscosity is represented by $G_\nu$and destruction turbulent viscosity represented by Y_ν. It must be note that since the turbulent kinetic energy is not modelled in the Sparat-Allmaras model, the last term in Equation (2.8) is ignored when predicting Reynolds stresses.

The turbulent viscosity is computed by Equation (2.10) :

$$\mu_t = \rho\tilde{\nu}f_{\nu 1} \tag{2.10}$$

Where $f_{\nu 1}$ indicates viscous damping function, it is calculated as follows:

$$f_{\nu 1} = \frac{\chi^3}{\chi^3 + C_{\nu 1}^3} \tag{2.11}$$

And

$$\chi = \frac{\tilde{\nu}}{\nu} \tag{2.12}$$

The default values of model constants are given below:

$$C_{b2} = 0.622, \qquad \sigma_{\tilde{\nu}} = 0.66, \quad C_{\nu 1} = 7.1$$

2.2.3.2 Realizable k-ε Turbulence Model

All of the k-ε turbulence models solve two modeled transport equations for turbulent kinetic energy (k) and turbulent dissipation rate (ε) hence k-ε models categorized under “two equations turbulence models”. Realizable k-ε turbulence model gets “realizable” title due to satisfy specific mathematical constraints for Reynolds stresses. Model is consistent with the physics of turbulent flows. The other k-ε turbulence models, RNG and Standard k-ε models are not realizable. Realizable k-ε model gives more accurate results for planar and round jets. Also realizable k-ε model provides excellent performance for flows that include rotation, separation, recirculation and boundary layers under strong adverse pressure gradients [23].

Transport equations of realizable k-ε turbulence model for k and ε have been given by Equation (2.13) and Equation (2.14) [23].

$$\frac{\partial}{\partial t}(\rho k) + \frac{d}{dx_j}(\rho k u_j) = \frac{\partial}{\partial x_j}\left[\left(\mu + \frac{\mu_t}{\sigma_k}\right)\frac{\partial k}{\partial x_j}\right] + \\ + G_k + G_b - \rho\varepsilon - Y_M + S_k \tag{2.13}$$

$$\frac{\partial}{\partial t}(\rho\varepsilon) + \frac{\partial}{\partial x_j}(\rho\varepsilon u_j) = \frac{\partial}{\partial x_j}\left[\left(\mu + \frac{\mu_t}{\sigma_\varepsilon}\right)\frac{\partial\varepsilon}{\partial x_j}\right] + + \rho C_1 S\varepsilon - \tag{2.14}$$

$$- \rho C_2 \frac{\varepsilon^2}{k + \sqrt{\nu\varepsilon}} + C_{1\varepsilon}\frac{\varepsilon}{k}C_{3\varepsilon}G_b + S_\varepsilon$$

Where:

$$C_1 = max\left[0.43, \frac{\eta}{\eta + 5}\right], \quad \eta = S\frac{k}{\varepsilon}, \quad S = \sqrt{2S_{ij}S_{ij}}$$

G_k indicates production of turbulent kinetic energy due to gradients of mean velocities. G_b indicates production of turbulent kinetic energy due to buoyancy. Increase of overall dissipation rate due to fluctuating dilatation in compressible turbulence is represented by Y_M. Turbulent Prandtl numbers for k and ε are indicated by σ_k and σ_ε. Finally, S_k and S_ε are user defined source terms while C_2 and $C_{1\varepsilon}$ are constants.

Similar to the other k-ε models, turbulent viscosity is defined as follows [23]:

$$\mu_t = \rho C_\mu \frac{k^2}{\varepsilon} \tag{2.15}$$

Another difference between realizable and other k-ε turbulence models is that C_μ is not a constant for realizable k-ε model. C_μ is calculated by equation (2.16) [23]:

$$C_\mu = \frac{1}{A_0 + A_s \frac{kU^*}{\varepsilon}} \tag{2.16}$$

Where

$$U^{*} = \sqrt{S_{ij}S_{ij} + \tilde{\Omega}_{ij}\tilde{\Omega}_{ij}} \tag{2.17}$$

In Equation (2.16), A_0 and A_0 are constants and they are given by

$$A_0 = 4.04, \quad A_s = \sqrt{6}cos\phi$$

Where

$$\phi = \frac{1}{3}cos^{-1}(\sqrt{6}W), \;\; W = \frac{S_{ij}S_{jk}S_{ki}}{\tilde{S}^3}, \;\; \tilde{S} = \sqrt{S_{ij}S_{ij}}, \;\; S_{ij} = \frac{1}{2}\left(\frac{\partial u_j}{\partial x_i} + \frac{\partial u_i}{\partial x_j}\right)$$

The other constants $C_{1\varepsilon}$,C_2, σ_k and σ_ε are used to ensure that model gives good results for standard flows. These model constants are given as follows [23];

$$C_{1\varepsilon} = 1.44, \quad C_2 = 1.9, \quad \sigma_k = 1.0, \quad \sigma_\varepsilon = 1.2$$

2.2.3.3 SST k-ω Turbulence Model

Similar to the k-ε models, k-ω turbulence models solve two transport equations for k and ω. SST k-ω was developed to improve accuracy of k-ω model in the near-wall region with the free-stream independence of k-ε model in the far field. The k-ε model formulation is converted into k-ω formulation to achieve this. SST k-ω is similar to standard k-ω model but SST k-ω model contains following enhancements [26]:

- The converted k-ε model and the standard k-ω model are multiplied by a blending function and both models are added together.
- A damped cross-diffusion derivative term is used in the ω transport equation.
- Calculation of turbulent viscosity is modified to cover transport of the turbulent shear stress.
- Different modelling constants are used.

These improvements increase reliability and accuracy of the k-ω model for various flow problems compared to standard k-ω model. Flows over an airfoil, adverse pressure gradient flows and transonic flows can be shown as examples [23].

Transport equations of SST k-ω model for k and ω are given by Equation (2.18) and Equation (2.19).

$$\frac{\partial}{\partial t}(\rho k) + \frac{\partial}{\partial x_i}(\rho k u_i) = \frac{\partial}{\partial x_j}\left(\Gamma_k \frac{\partial k}{\partial x_j}\right) + \tilde{G}_k - Y_k + S_k \tag{2.18}$$

$$\frac{\partial}{\partial t}(\rho\omega) + \frac{d}{dx_i}(\rho\omega u_i) = \frac{\partial}{\partial x_j}\left(\Gamma_\omega \frac{\partial \omega}{\partial x_j}\right) + \tag{2.19}$$

$$+G_\omega - Y_\omega + D_\omega + S_\omega$$

In these equations, G_k indicates generation of turbulent kinetic energy due to gradients of mean velocities. G_ω indicates generation of specific dissipation rate. Effective diffusivities of k and ω are represented by Γ_k and Γ_ω. Dissipation of k and ω due to turbulence are represented by Y_k and Y_ω. The cross-diffusion term is indicated by D_ω. Finally, S_k and S_ω represent user defined source terms.

The effective diffusivities are calculated by using equation (2.20) and (2.21):

$$\Gamma_k = \mu \frac{\mu_t}{\sigma_k} \tag{2.20}$$

$$\Gamma_\omega = \mu \frac{\mu_t}{\sigma_\omega} \tag{2.21}$$

σ_k and σ_ω indicate turbulent Prandtl numbers for k and ω and the turbulent viscosity is calculated as follows:

$$\mu_t = \frac{\rho k}{\omega} \frac{1}{max\left[\frac{1}{\alpha^*}, \frac{SF_2}{a_1 \omega}\right]} \tag{2.22}$$

The strain rate magnitude is represented by S and turbulent Prandtl numbers for k and ω are calculated as follows:

$$\sigma_k = \frac{1}{\frac{F_1}{\sigma_{k,1}} + (1 - F_1)/\sigma_{k,2}} \tag{2.23}$$

$$\sigma_k = \frac{1}{\frac{F_1}{\sigma_{w,1}} + (1 - F_1)/\sigma_{w,2}} \tag{2.24}$$

Where α^* is a coefficient that damps turbulent viscosity to yield a low-Reynolds number correction. It is calculated by equation 2.16:

$$\alpha^* = \alpha_\infty^* \left(\frac{\alpha_0^* + Re_t/R_k}{1 + Re_t/R_k}\right) \tag{2.25}$$

Where

$$Re_t = \frac{\rho k}{\mu \omega} \tag{2.26}$$

The blending functions F_1 and F_2 are computed from given equations below:

$$F_1 = \tanh\left(\Phi_1^4\right) \tag{2.27}$$

$$\Phi_1 = min\left[max\left(\frac{\sqrt{k}}{0.09\omega y}, \frac{500\mu}{\rho y^2 \omega}\right), \frac{4\rho k}{\sigma_{w,2} D_\omega^+ y^2}\right] \tag{2.28}$$

$$D_{\omega}^{+} = max\left[2\rho\frac{1}{\sigma_{w,2}}\frac{1}{\omega}\frac{\partial k}{\partial x_j}\frac{\partial \omega}{\partial x_j}, \frac{500\mu}{\rho y^2\omega}\right] \tag{2.29}$$

$$F_2 = \tanh\left(\Phi_2^2\right) \tag{2.30}$$

$$\Phi_2 = max\left[2\frac{\sqrt{k}}{0.09\omega y}, \frac{500\mu}{\rho y^2\omega}\right] \tag{2.31}$$

SST k-ω turbulence model constants, that are mentioned earlier, are given as follows:

$$R_k = 6, \quad \alpha_0^* = 0.024, \quad a_1 = 0.31$$

$$\sigma_{k,1} = 1.176, \quad \sigma_{k,2} = 1, \quad \sigma_{\omega,1} = 2, \quad \sigma_{\omega,2} = 1.168$$

2.3 Sub-Domain Motion Modelling

In this part, cell zone conditions and mesh deformation theories that are used to simulate motion of AUV during hydrodynamic tests will be given.

2.3.1 Mesh Deformation

Solution of a time dependent dynamic motion requires deformation of fluid domain due to displacement of the model. FLUENT has a capability of the spring based mesh smoothing and this feature of FLUENT is used to simulate pure heave motion which is described in Section 1.2.3.1. Displacement of the fluid sub-domain is chosen according to reference documents in literature. A user defined function (UDF) is written in C language to define motion for FLUENT. In addition, a re-meshing command is defined to protect mesh quality.

Mesh edges are considered as springs in spring based mesh motion so that mesh edges emerge a network of springs. After any displacement of a boundary, springs network ensures equilibrium of state of the mesh by deforming mesh. Displacement of a boundary node generates a force that can be calculated on a mesh node by using Hook's law as follows [23]:

$$\vec{\mathrm{F}}_i = \sum_{j}^{n_i} k_{ij}(\Delta\vec{x}_j - \Delta\vec{x}_i) \tag{2.32}$$

Where $\Delta\vec{x}_i$ and $\Delta\vec{x}_j$ are node displacements, k_{ij} is spring constant of between node i and node j and n_i is the number of neighbor nodes of node i. Spring constant between node i and node j can be computed by following equation:

$$k_{ij} = \frac{1}{\sqrt{\left|\vec{x}_i - \vec{x}_j\right|}} \tag{2.33}$$

Spring constant value determines effected zone and varies between 0 and 1. As spring constant value approaches to 0, only neighboring nodes of displaced node are affected by smoothing. On the contrary, as spring constant value approaches to 1, further nodes of displaced node are affected by smoothing [23].

Spring based smoothing on a cylindrical domain has been illustrated by Figure 2.1:

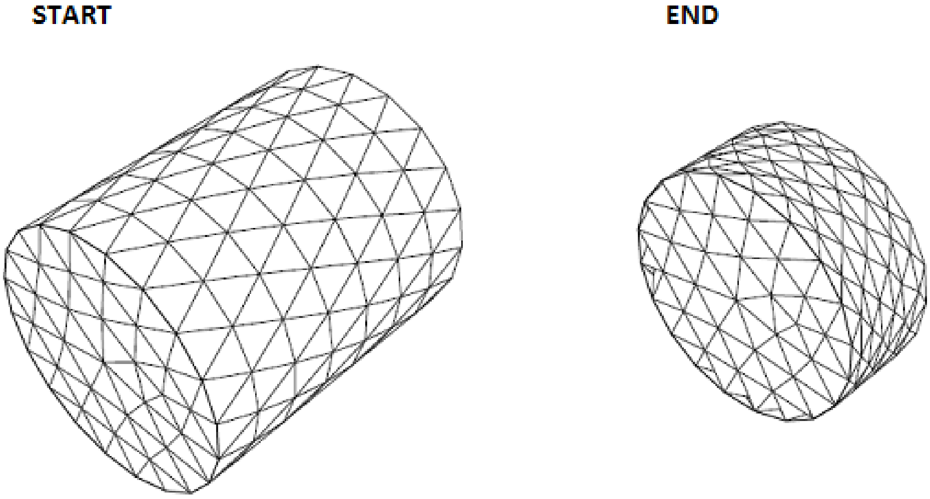

Figure 2.1 Spring Based Smoothing on a Cylindrical Domain [23]

2.3.2 Moving Reference Frame

In general, flow problems that involve moving parts require unsteady solutions. However, flow problems which are unsteady in stationary frame but steady with respect to a steadily rotating frame can be model as a steady-state problem by using FLUENT’s moving reference frame feature. In details, mesh motion are not required for CFD analysis that are modelled with moving reference frame. It can be noted that “steadily rotating frame” statement has been used to define a constant rotation speed.

Stationary and moving reference frames are illustrated in Figure 2.2:

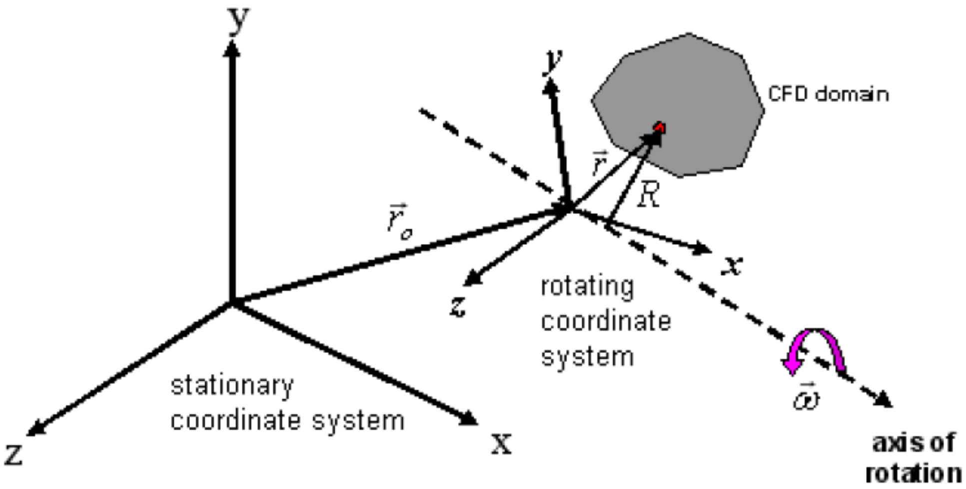

Figure 2.2 Stationary and Moving Reference Frames [23]

Equations of motion are modified to define additional terms that occur due to coordinate system transformation from stationary to moving reference frame.

As shown in Figure 2.2, $\vec{\omega}$ is constant angular velocity and $\overrightarrow{r_0}$ is position vector that locates origin of the rotating system. The rotation axis is defined by using a unit vector. Where $\hat{a}$ is the unit vector:

$$\vec{\omega} = \omega\hat{a} \tag{2.34}$$

An arbitrary point in the CFD domain is located by a position vector $\vec{r}$ with respect to the moving reference frame.

The fluid velocities which are transformed from the stationary frame to moving reference frame can be calculated by equation (2.35):

$$\vec{v}_r = \vec{v} - \vec{u}_r \tag{2.35}$$

Where

$$\vec{u}_r = \vec{\omega} \times \vec{r} \tag{2.36}$$

In these equations, $\vec{v}_r$ represents relative velocity (velocity according to rotating coordinate system), $\vec{v}$ represents the absolute velocity (velocity according to stationary coordinate system) and $\vec{u}_r$ represents whirl velocity (velocity because of the rotating frame). These transformed fluid velocities are used to modify governing equations.

Moving reference frame (MRF) cell zone condition can be defined for the entire fluid domain or sub-domains. A multi domain CFD application is illustrated in Figure 2.3.

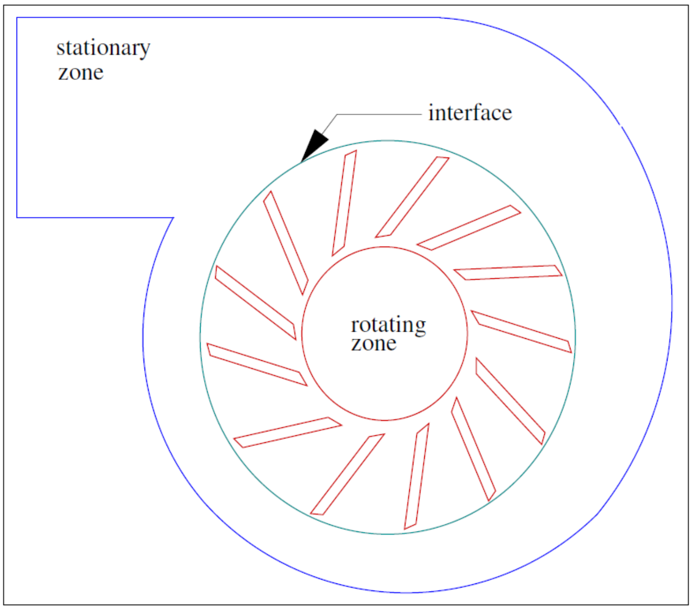

Figure 2.3 A Multi Domain CFD Application with MRF Cell Zone Condition (Blower Wheel and Casing) [23]

2.3.3 Sliding Mesh

In the case of unsteady flow field, a time-dependent solution is required. MRF technique is not capable of modelling unsteady motions and MRF neglects unsteady interactions such as potential, wake and shock interactions. Sliding mesh technique must be used to model unsteady rotations or translations and to capture unsteady interactions. The sliding mesh model is the most accurate method to simulate flows in a domain that contains multiple moving zones. Two or more cell zones are used in sliding mesh technique. Each zone has at least one interface zone so that two interface zones separate zones from each other. The two cell zones slides along these mesh interfaces [27].

As shown in Figure 2.4 an interior zone emerges between two interface zones due to intersection of mesh interfaces.

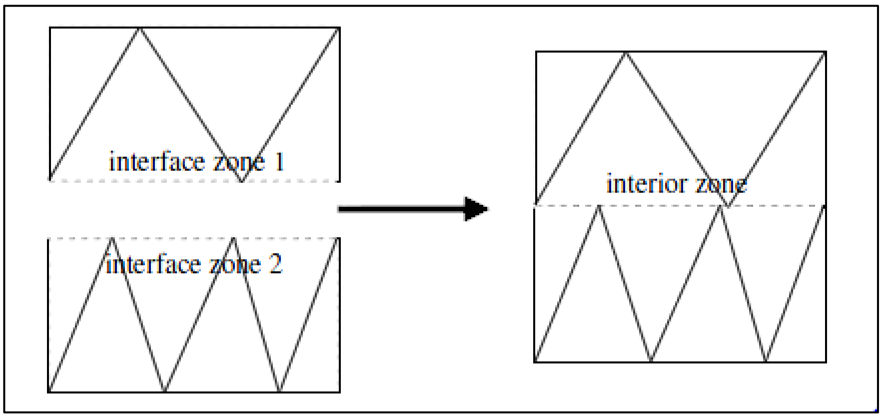

Figure 2.4 Two Dimensional Mesh Interface Intersection [27]

Flux across the interface zones are calculated by using the faces that are formed by intersection points so that initial cell faces on the mesh interfaces are ignored [27].

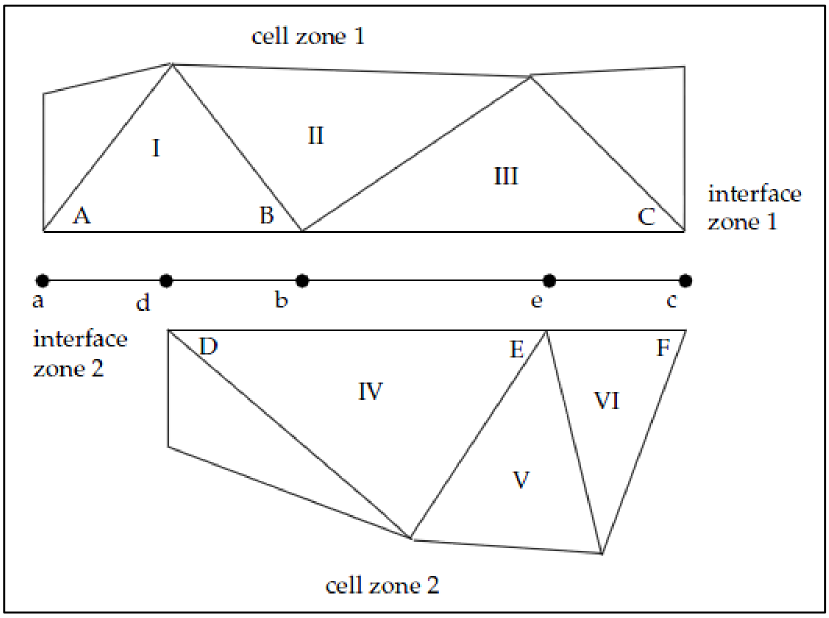

Figure 2.5 Two Dimensional Mesh Interface [27]

For the mesh interface which is shown in Figure 2.5, flux across the interface into cell IV is computed by using face d-b and face b-e instead of using face D-E.

2.4 Solver Type

There are two types of flow solvers that are available in FLUENT; pressure based and density based solvers. Originally, pressure-based solver has been developed for low-speed incompressible flows and density-based solver has been developed for high-speed compressible flows. However, both solver types are enhanced to cover a wide range of flows beyond their original purpose in time [23].

In this study, fluid material is water for all CFD analyses hence it can be assumed that flow is incompressible. Taking this condition into consideration, pressure-based solver is chosen for analyses.

An algorithm which is classified under the general class of methods called the projection method is used in the pressure-based solver [28]. A pressure equation is solved in order to achieve velocity field in projection method. The pressure equation is derived from continuity and momentum equations where achieved velocity field is corrected by pressure and it satisfies continuity. The governing equations are non-linear and coupled to each other so that solution process continues iteratively until the solution converges [23].

In addition, there are two different pressure-based algorithms are available in FLUENT. General background of these algorithms will be given in this part.

2.4.1 The Pressure-Based Segregated Algorithm

The governing equations are solved sequentially in the pressure-based segregated algorithm. As mentioned before, governing equations must be solved iteratively to obtain a converged solution since the governing equations are non-linear and coupled. In segregated algorithm, governing equations are solved one after another to obtain solution variables. Since the equations are decoupled or segregated in solution, algorithm called as “segregated”. The pressure-based segregated algorithm is memory-efficient because equations need to be stored once at a time. On the other hand, the solution convergence needs more iteration because of the decoupled solution.

Steps of each iteration in the pressure-based segregated algorithm are illustrated in Figure 2.6.

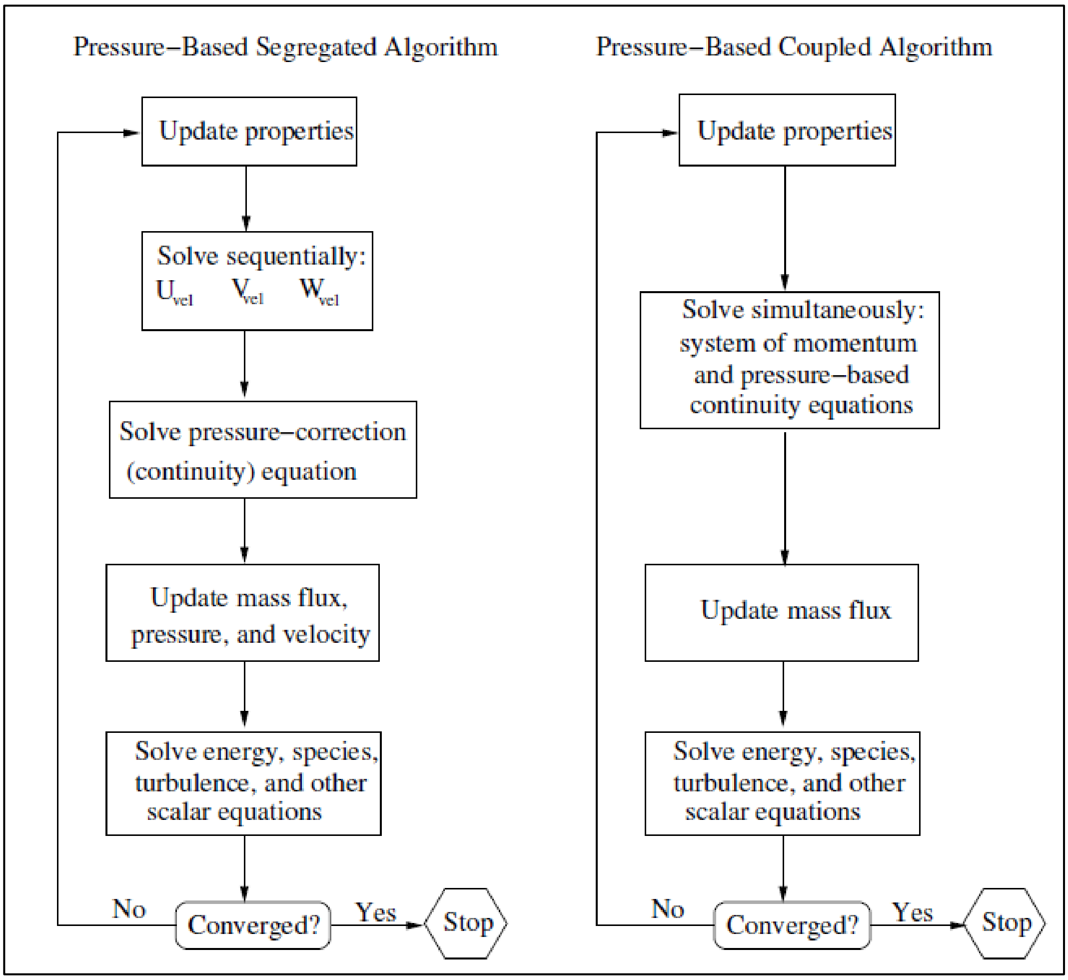

Figure 2.6 Overview of the Pressure-Based Solvers [23]

2.4.2 The Pressure-Based Coupled Algorithm

Difference of pressure-based coupled algorithm is that coupled algorithm solves a coupled system of equations consisting pressure-based continuity and momentum equations [23]. As shown in Figure 2.6, in coupled algorithm, step 2 and step 3 of segregated algorithm are replaced with a single step wherein a coupled system of governing equations is solved. The other steps of coupled algorithm are same compared to the segregated algorithm.

CHAPTER 3

TEST CASE MODELS

Sample designs whose geometric specifications and experimental data are available in open sources are called test cases. Test cases are used for code validation and modelling technique verification. Two different test cases are used for CFD analyses in this study.

In this part, detailed information about test case models which have been used for CFD analyses will be given. Autosub AUV model is used for simulation of straight-line towing, RA and PMM tests while DARPA AUV model is used for only straight-line towing tests.

3.1 Autosub AUV

The Autosub AUV designed and developed for global monitoring and for marine science programs by UK National Environment Research Council in 1988 [13]. Autosub AUV can gather information about water and its location such as temperature, photosynthetic active radiation, depth and saltiness by using sensors that can measure physical, biological and chemical properties.

¾ scale Autosub model is used for hydrodynamic tests in referenced studies hence scaled Autosub model is used for CFD analyses. Geometric specifications of ¾ scale Autosub model are given in Table 3.1:

Table 3.1 Geometric Specifications of Autosub Model [29, 30]

Length	5.2 m
Diameter	0.67 m
Nose Length	0.77 m
Nose Shape	Elliptic
Body Length	2.87 m
Body Cross-Section Area	0.35 m^2
Aft-body Length	1.56 m
CG Distance from Nose	2.347 m
Tail Span (Tip to Tip)	0.88 m
Tail Tip Chord Length	0.21 m
Sweep Angle (Leading Edge)	11.13^0
Sweep Angle (Trailing Edge)	0^0
Tail Airfoil	NACA0015

Autosub has four tails in "+" configuration. Solid model and tail configuration of Autosub AUV are shown in Figure 3.1:

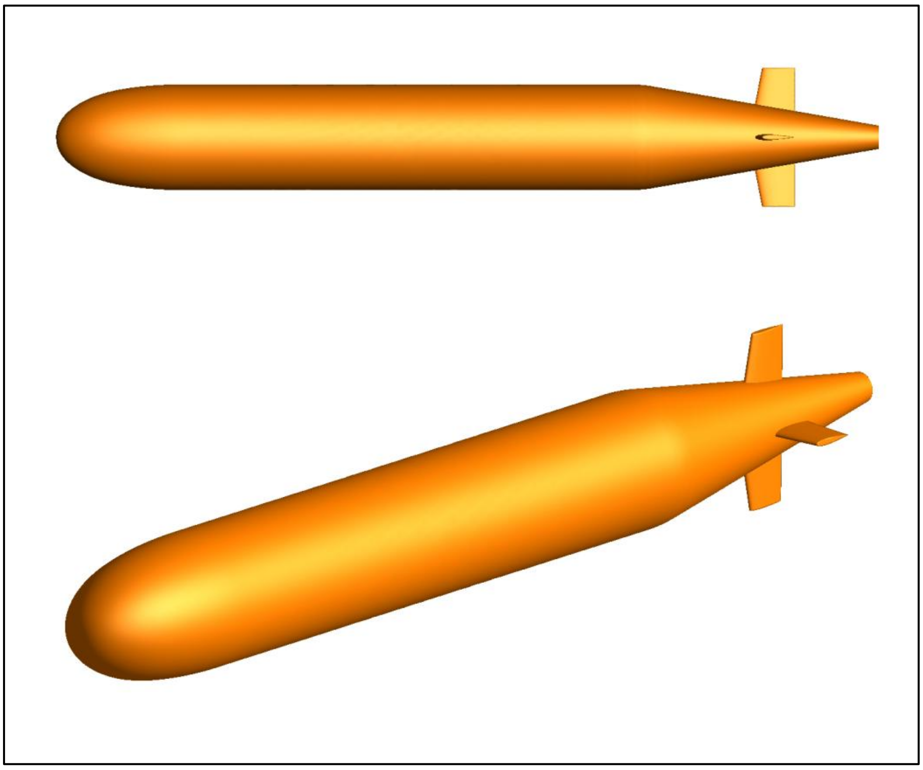

Figure 3.1 Autosub Solid Model and Tail Configuration

Experimental data of Autosub model is obtained from studies of Kimber et al. [13, 31].

3.2 DARPA AUV

The DARPA SUBOFF project has been funded by Defense Advanced Research Projects Agency to assist in the development of advanced submarines. In detail, the purpose of this project was to provide experimental results for development of CFD methods.

Different configurations of DARPA model are designed at David Taylor Research Center. All configurations have same axisymmetric body so that configurations are named according to the appendages of the body. In this study, Configuration 5 of DARPA SUBOFF model, which consists of an axisymmetric body and four tails, is used for CFD analyses. Geometric specifications of DARPA model are given in Table 3.2:

Table 3.2 Geometric Specifications of DARPA Configuration 5 Model [32]

Length	4.356 m
Diameter	0.508 m
Nose Length	1.016 m
Body Length	2.229 m
Body Cross-Section Area	0.203 m^2
Aft-body Length	1.111 m
CG Distance from Nose	2.009 m
Tail Span (Tip to Tip)	0.508 m
Tail Tip Chord Length	0.152 m
Sweep Angle (Leading Edge)	25.2^0
Sweep Angle (Trailing Edge)	0^0

Similar to the Autosub AUV, DARPA model has four tail in “+” configuration too. Solid model and tail configuration of DARPA model are shown in Figure 3.2:

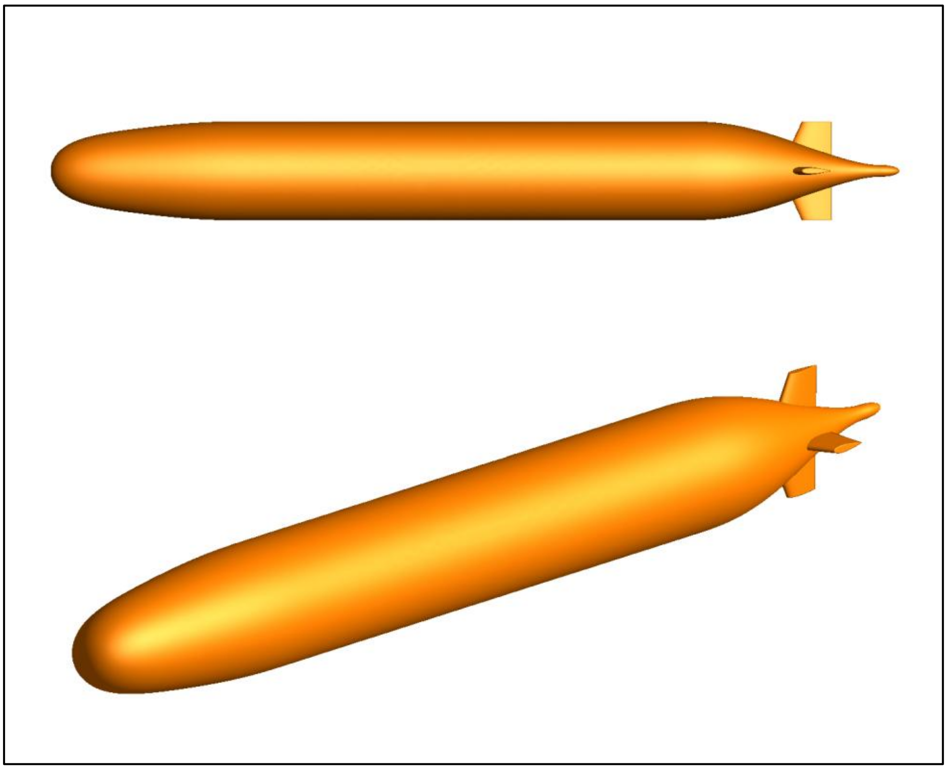

Figure 3.2 DARPA Solid Model and Tail Configuration

Detailed information about geometry of DARPA SUBOFF models can be reached from referenced document [32]. In addition experimental data of DARPA model is obtained from studies of Roddy. [12]

CHAPTER 4

SIMULATIONS OF STRAIGHT-LINE TOWING TESTS

In this study, particular motions in hydrodynamic tests are simulated by using CFD methods. In this part, details of CFD simulations of straight-line towing tests will be given. Besides, details of RA and PMM CFD simulations will be given in next chapters.

Straight-line towing test is simulated for Autosub and DARPA test case models, RA test and PMM test are simulated for Autosub test case model. RA tests are simulated for constant angular velocity and constant angular acceleration. Moreover, PMM test simulations consist of pure heave motion simulation and combined motion simulation which is combination of pure heave and pure pitch motions.

Hydrodynamic problems are described according to a different coordinate system compared to the aerodynamic problems. So that a common coordinate system in hydrodynamic literature is used in this study. The used hydrodynamic coordinate system is shown in Figure 4.1:

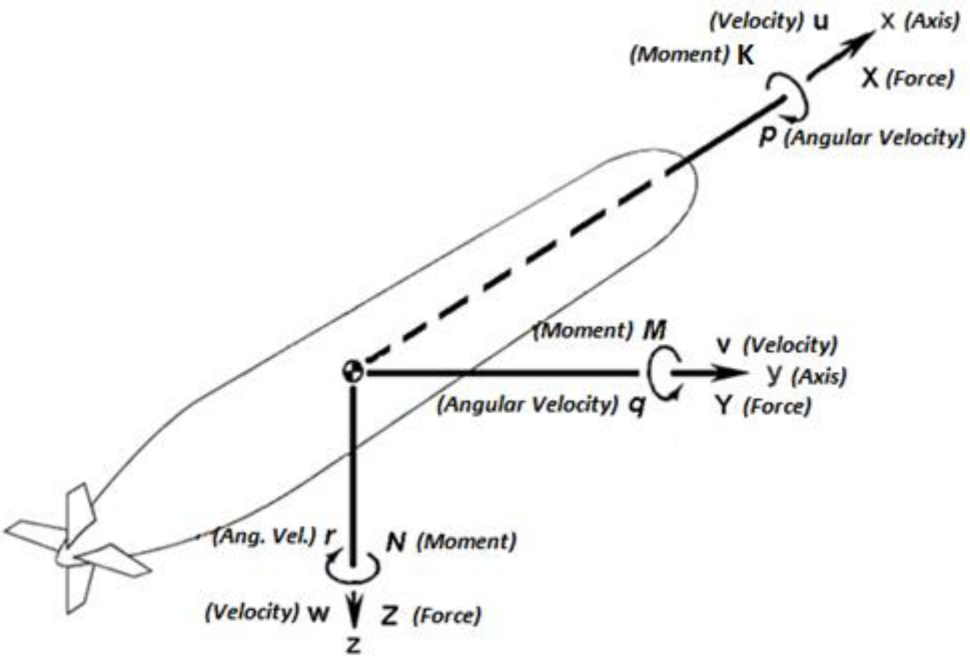

Figure 4.1 Hydrodynamic Coordinate System

In coordinate system, X, Y, Z represent forces and K, M, N represent moments on x, y, z directions. In addition, where θ is a quantity θ' represents non-dimensional form of it. Parameters which are used to calculate non-dimensional coefficients are given in Table 4.1:

Table 4.1 Non-dimensionalization Parameters

Coefficient	**Parameter**
Forces	$^1/_2\,\rho V^2 L^2$
Moments	$^1/_2\,\rho V^2 L^3$
Z'_{w}	$w\,^1/_2\,\rho V L^2$
M'_{w}	$w\,^1/_2\,\rho V L^3$
$\mathrm{Z}'_{\dot{\mathrm{w}}}$	$\dot{w}\,^1/_2\,\rho L^3$
$\mathrm{M}'_{\dot{\mathrm{w}}}$	$\dot{w}\,^1/_2\,\rho L^4$
Z'_{q}	$q\,^1/_2\,\rho V L^3$
M'_{q}	$q\,^1/_2\,\rho V L^4$
$\mathrm{Z}'_{\dot{\mathrm{q}}}$	$\dot{q}\,^1/_2\,\rho L^4$
$\mathrm{M}'_{\dot{\mathrm{q}}}$	$\dot{q}\,^1/_2\,\rho L^5$
w'	V
$\dot{\mathrm{w}}'$	V^2/L
q'	V/L
$\dot{\mathrm{q}}'$	V^2/L^2

The ρ indicates fluid density, V indicates free-stream velocity and L indicates length of model.

As mentioned before two different test case models are used for straight-line towing test CFD simulations and detailed information about CFD modelling of towing tests and CFD analyses results will be given in this part.

4.1 Autosub Model Straight-line Towing Test Simulation

Steps of CFD simulation process can be listed as follows:

- Drawing solid model and generating surface mesh by using GAMBIT commercial program.
- Defining boundary conditions in GAMBIT.
- Importing surface mesh into TGRID commercial program and generating boundary layer and volume meshes.
- Importing volume mesh into FLUENT commercial program and adjusting solver settings.
- Defining cruise conditions and simulation.

4.1.1 Grid Generation

Unstructured grids define complex geometries better than the structured grids. Therefore unstructured grids are generated with tetrahedron elements for all CFD simulations in this study. Moreover, triangle elements are used for surface grid and prism/wedge elements are used for boundary layer grids. Grid elements are shown in Figure 4.2:

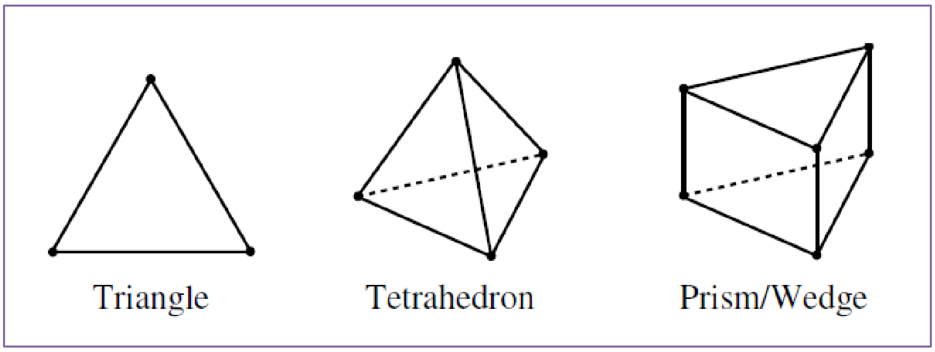

Figure 4.2 Grid Element Types [27]

In addition, grid independence study is done to get optimum number of grid elements.

4.1.1.1 Grid Independence Study

Four different grids which have unequal number of elements are generated to select the appropriate grid. It is predicted that flow properties change considerable where diameter transition occurs and where surface interactions are effective (body-tail connection locations). Therefore, elements which have smaller size are used for these locations while generating surface grids. Then Boundary layer grids are generated around model. Boundary layer grid consists of 20 layers. First 10 of layers grow exponentially and the other 10 layers grow to ensure that aspect ratio of last layer is %50. Far regions of flow domain are affected less by flow changes around model. Hence volume grids are generated with linearly growing cell size from model surface to outer regions. Generated surface and volume grids are illustrated in Figure 4.3:

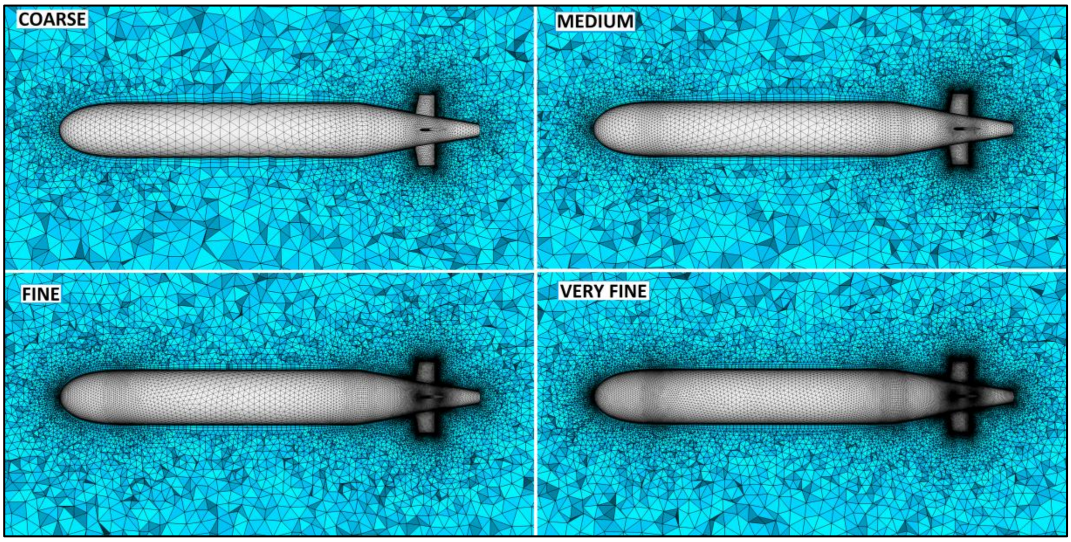

Figure 4.3 Coarse, Medium, Fine and Very Fine Surface and Volume Grids

Element numbers of coarse, medium, fine and very fine grids are given in Table 4.2:

Table 4.2 Element Numbers of Autosub Grids According to Grid Density

Grid Density	Number of Surface Grid Elements	Number of Prism/Wedge Elements	Number of Tetrahedron Elements
Coarse	13,864	277,280	741,909
Medium	27,020	540,520	1,143,228
Fine	59,258	1,185,160	1,882,701
Very Fine	95,728	1,914,560	2,705,085

Straight-line towing test of Autosub model is simulated with generated grids. Cruise conditions of test case study are given in Table 4.3:

Table 4.3 Cruise Conditions for Autosub Towing Test Simulations

Velocity (m/s)	2.69
Angles of Attack (^{o})	0, 2, 4, 6, 8, 10
Ambient Pressure (Pa)	150277

CFD simulations are done for given cruise conditions. Calculated force and moment coefficients on the Z direction are given in Figure 4.4 and Figure 4.5:

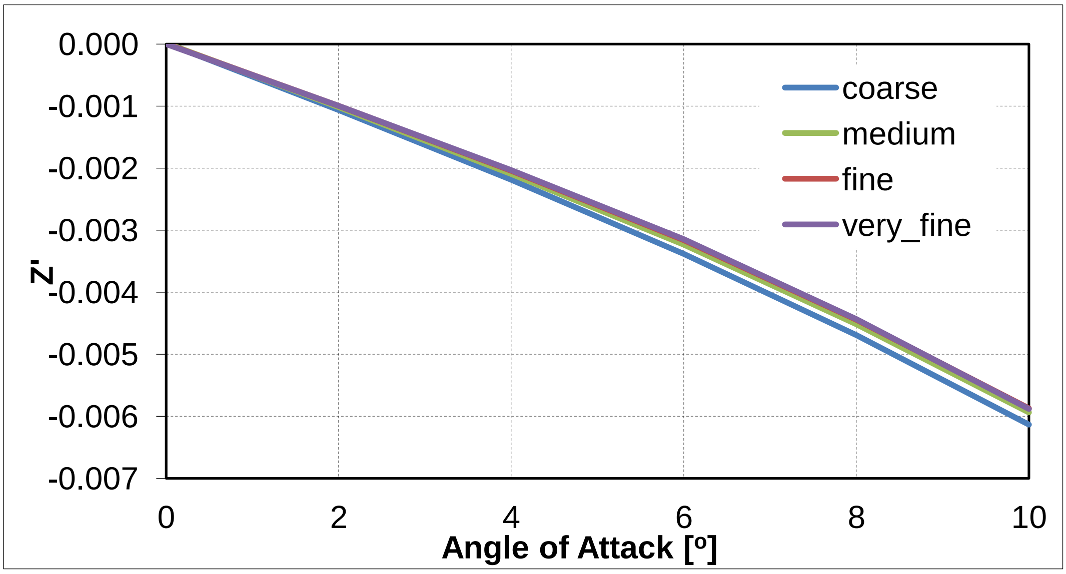

Figure 4.4 Autosub AUV Z Force Coefficient With Respect to AOA for Different Grids

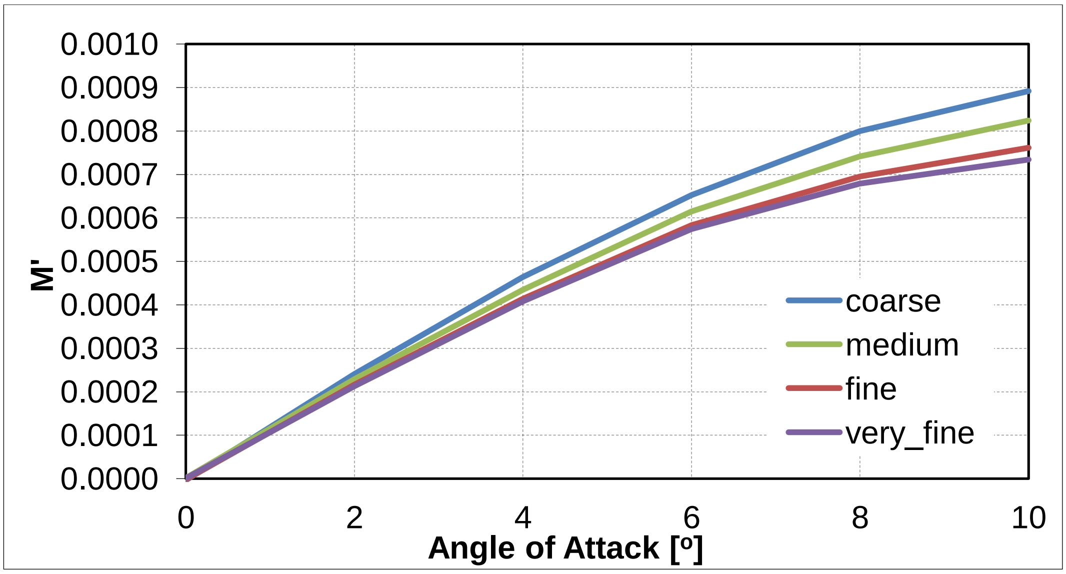

Figure 4.5 Autosub AUV Pitch Moment Coefficient With Respect to AOA for Different Grids

Results are converged after using fine grid for solutions. Fine and very fine grids provides grid independence but fine grid has less number of cells. Therefore fine grid is chosen for CFD analyses to minimize computational time.

Fine surface grid is shown in Figure 4.6:

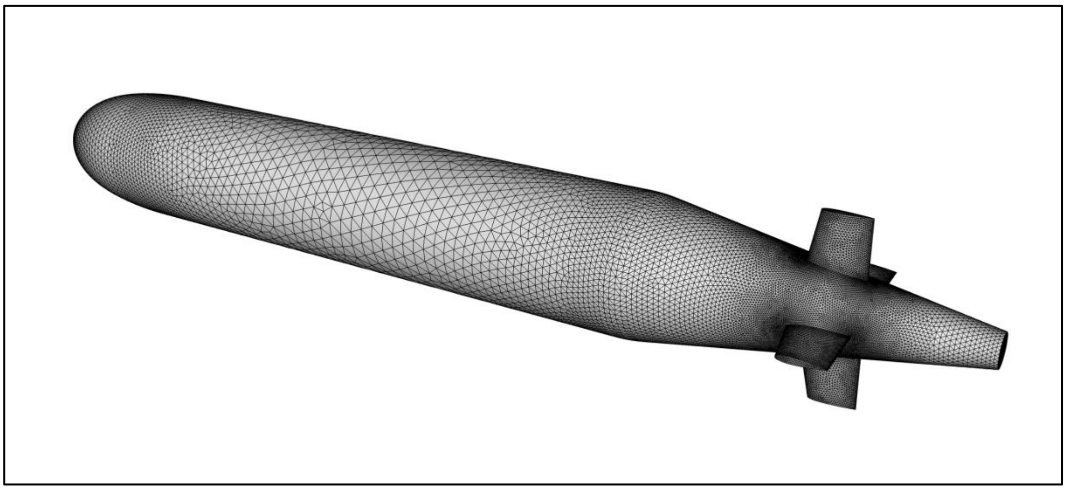

Figure 4.6 Fine Surface Grid for Autosub Model

Fine boundary layer and volume grids are shown in Figure 4.7 and Figure 4.8:

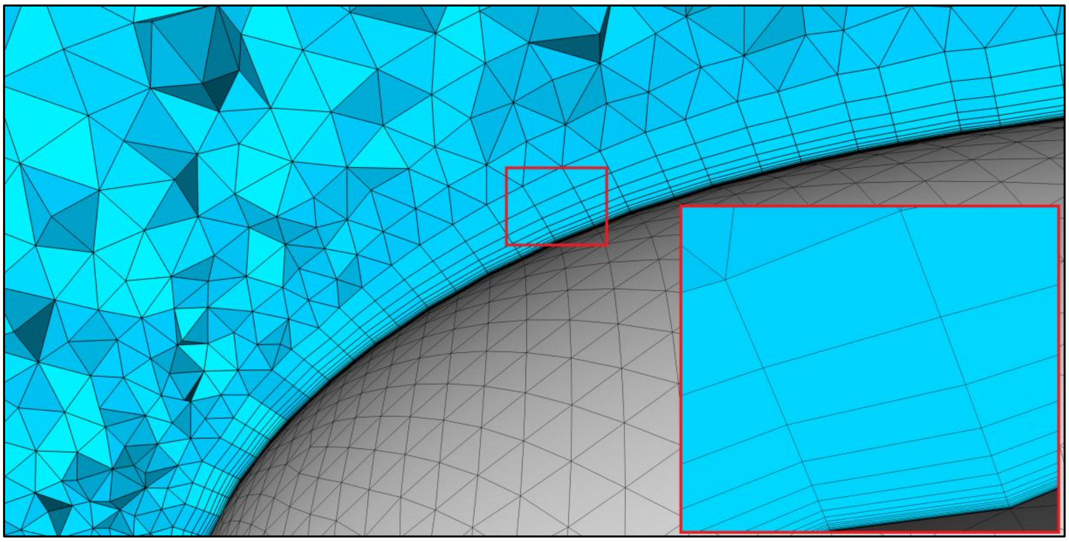

Figure 4.7 Fine boundary Layer Grid for Autosub Model

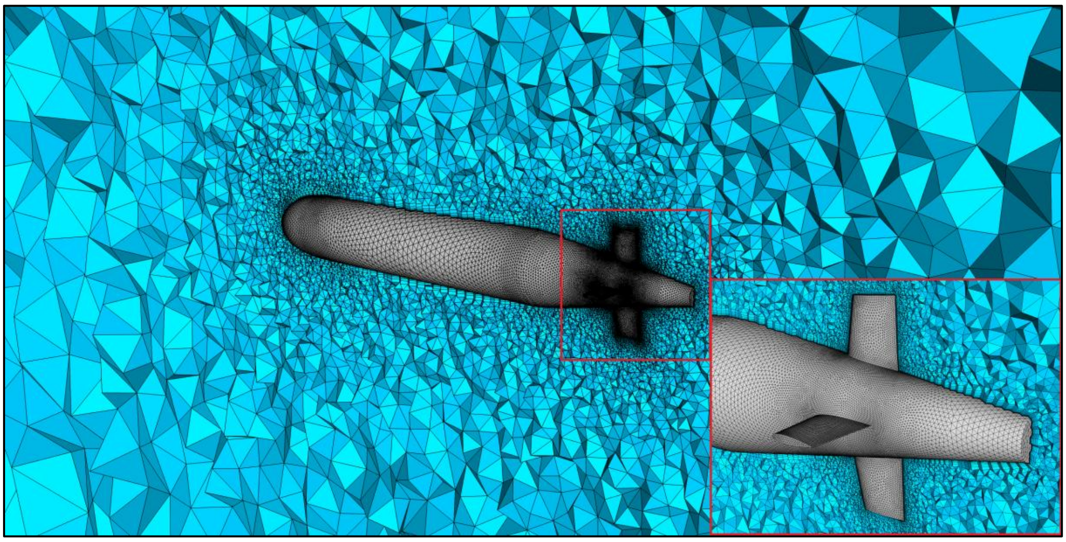

Figure 4.8 Fine Volume Grid and Detailed Tail Surfaces Grids for Autosub Model

Fine grid is used as a reference grid for the other hydrodynamic test simulations of Autosub Model. Hence grid independence study is not repeated.

4.1.1.2 Boundary Layer Analysis

Turbulent boundary layer consists of two different regions which are inner region and outer region. Also inner region is separated in three different groups and each group behaves differently. A very thin and closest layer to surface is called as “viscous sublayer”. Outer layer of inner region is called as “fully turbulent zone” and the zone between viscous sublayer and fully turbulent is called as “buffer zone”. Outer region comes after fully turbulent zone of inner region [33].

These regions are classified according to non-dimensional velocity (u^+) and surface spatial coordinate (y^+). These non-dimensional quantities are calculated as follows [33]:

$$u^+ = \frac{u}{u_r} \tag{4.1}$$

And

$$y^+ = y\frac{u_r}{\nu} \tag{4.2}$$

Where u_r is friction velocity and ν is kinematic viscosity, u_r is defined by Equation (4.3).

$$u_r = \sqrt{\frac{\tau_w}{\rho}} \tag{4.3}$$

And τ_w is wall shear stress and ρ is fluid density. Relation between turbulent boundary layer regions and y^+ have been given in Table 4.4:

Table 4.4 Relation between Boundary Layer Regions and y^+

$y^+ < 2\text{-}8$	Viscous Sublayer
$2\text{-}8 < y^+ < 2\text{-}50$	Buffer Zone
$y^+ > 50$	Fully Turbulent Zone
$y^+ < 100\text{-}400$	Inner Region
$y^+ > 100\text{-}400$	Outer Region

In addition to turbulence model, “enhanced wall treatment” approach has been used to model turbulence near wall boundaries. The y^+ value should be in constraints of fully turbulent region for “standard wall function” but y^+ value should be in constraints of viscous sublayer for enhanced wall treatment approach [23]. Therefore in accordance with enhance wall treatment approach, obtaining y^+ value as 1 is aimed. To achieve that first height value (y) must be calculated carefully during grid generation.

There are several first height prediction methods depends on y^+. In this study Equation (4.4) is used for calculation [33].

$$y = 6 \times \left(\frac{Re}{L}\right)^{\frac{-7}{8}} \times \left(\frac{L}{2}\right)^{\frac{1}{8}} \times y^+ \tag{4.4}$$

In equation, L represents length of model.

Predicted and fine grid pre-solution y^+ values are compared iteratively until the consistency is ensured. Results of y^+ values for chosen grid are given in Figure 4.9:

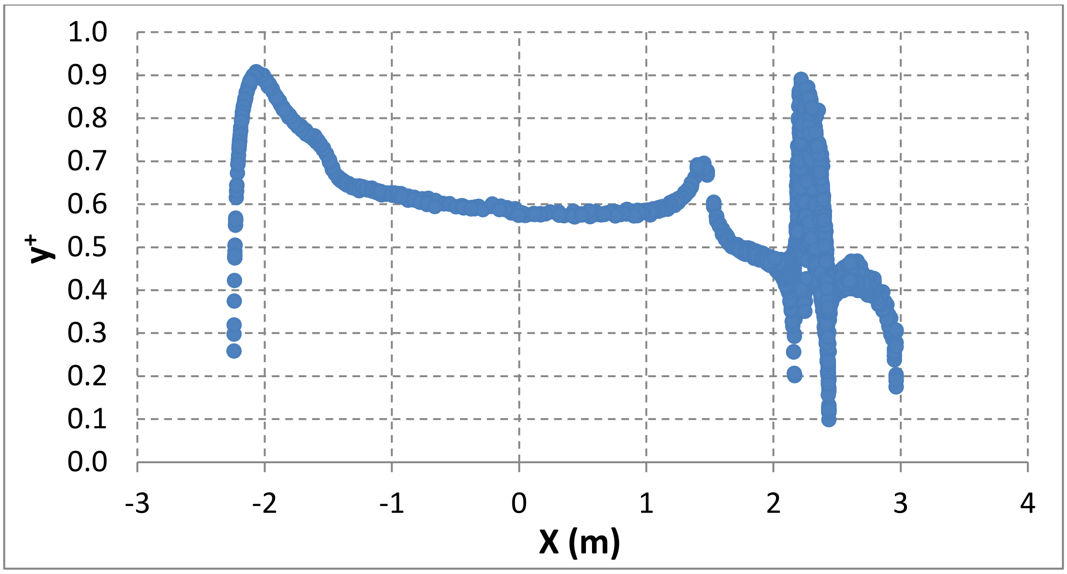

Figure 4.9 y+ Values for Autosub Grid

Obtained y^+ values are less than aimed value at all points. Hence boundary layer grid is fine enough for Autosub CFD simulations.

4.1.2 Boundary Conditions

Flow domain is defined large enough to minimize flow effects between model and boundaries. Front face, upper face, lower face and side faces are constrained at 15×L distance from model while back face is constrained at 25×L distance from model. Velocity inlet boundary condition is defined for front and lower faces, pressure outlet boundary condition is defined for back and upper faces, symmetry boundary condition is defined for side faces and wall boundary condition is defined for model surfaces. Flow domain and defined boundary conditions are illustrated in Figure 4.10:

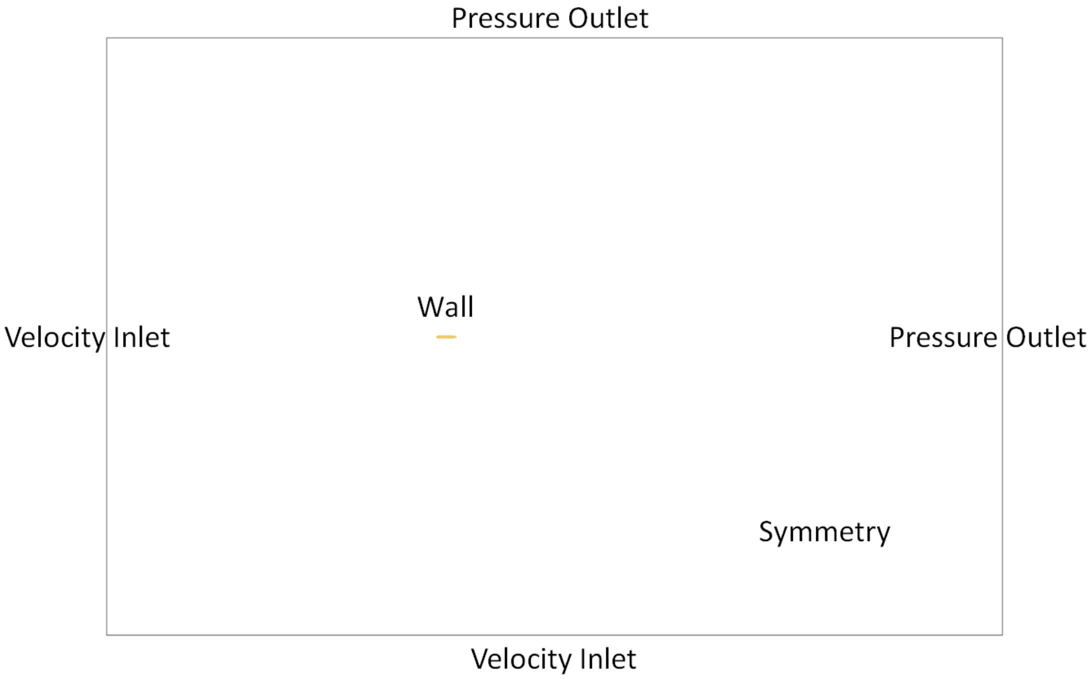

Figure 4.10 Flow Domain Boundary Conditions for Towing Tests

4.1.2.1 Wall Boundary Condition

It is a boundary condition which is used to separate fluid and solid regions from each other. No-slip wall boundary condition is defined for viscous flows [27]. In this study, wall boundary condition is defined for all of the model surfaces.

4.1.2.1.1 Symmetry Boundary Condition

This boundary condition can be used to define physically symmetric problems. Also it can be used to define wall conditions without shear stress. It is assumed that flux does not across the symmetry boundary condition. In this case, normal velocity component is zero (there is no convective flux) and normal gradients of all variables are zero (there is no diffusive flux) [27].

4.1.2.2 Velocity Inlet Boundary Condition

This boundary condition is used to define flow velocity and relevant scalar flow properties at flow inlets. The total pressure is not constrained hence pressure rises to value which is necessary to provide specified velocity distribution. Therefore it is intended for incompressible flows and in the case of its use in compressible flows non-physical results occur because of unconstrained pressure floating [27].

4.1.2.3 Pressure Outlet Boundary Condition

Pressure outlet boundary condition is used to define static pressure at flow outlets but specified pressure value is used only while the flow is subsonic. When the flow become locally supersonic, the specified pressure is no longer used and all flow properties are extrapolated from interior flow [27].

4.1.3 CFD Simulation Results and Turbulence Model Selection

Autosub straight-line towing test is simulated for cruise conditions given in Table 4.3. Steady-state CFD analyses are performed for three different turbulence models to select appropriate turbulence model for the rest of the hydrodynamic CFD analyses. CFD results (hydrodynamic forces and moments on Z direction) are compared with experimental data and given in Figure 4.11 and Figure 4.12 [31]:

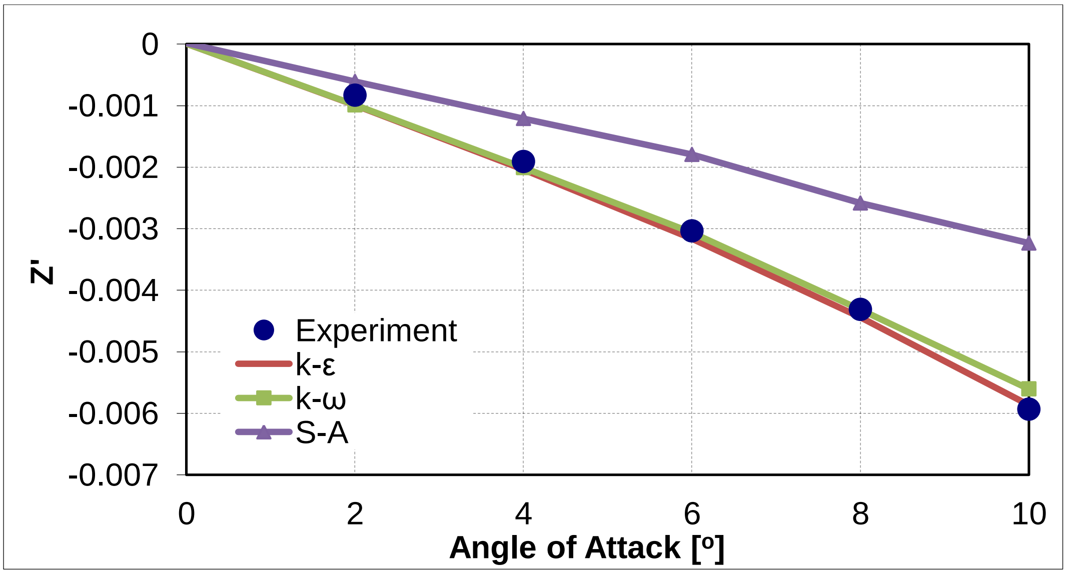

Figure 4.11 Autosub Model Z Force Coefficient Results and Experimental Data With Respect to AOA [31]

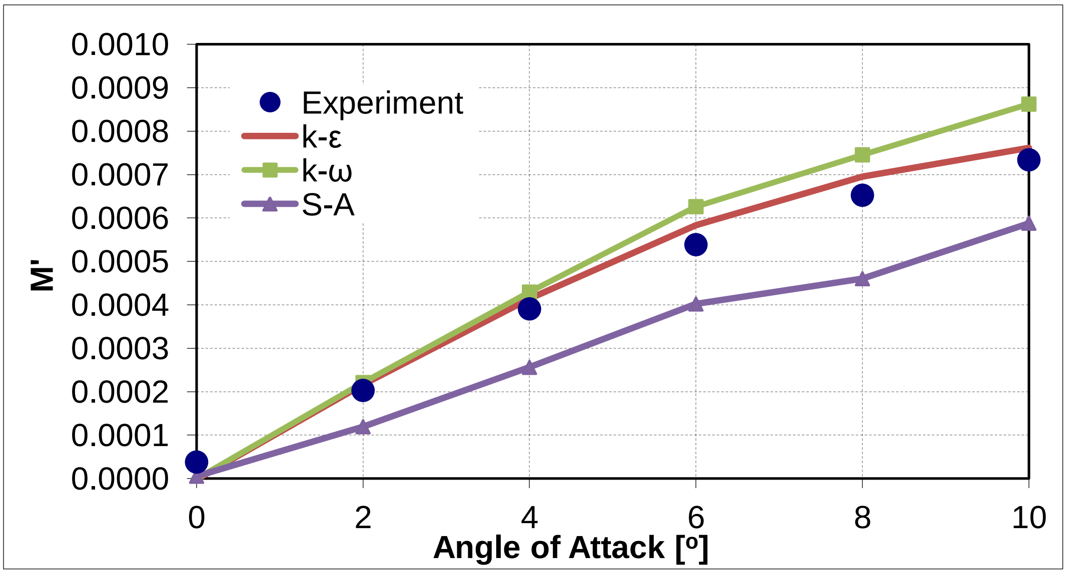

Figure 4.12 Autosub Model Pitch Moment Coefficient Results and Experimental Data With Respect to AOA [31]

As shown in figures, solutions obtained by k-ε turbulence model are more accurate than solutions of the other two models compared to the experimental data. Using k-ε model for rest of the study will be appropriate. For an instance, CFD results at 10°

angle of attack are examined and error percentages of comparisons between CFD results and experimental data are given in Table 4.5:

Table 4.5 Error Percentages of Turbulence Models according to the Results of Towing Test Simulation (α=10°)

	Error Percentage (%)		
Coefficients	k-ε	k-ω	S-A
Z'	1.1	5.6	45.5
M'	3.8	17.5	19.9

Results of k-ε model are in good agreement with experimental data and satisfy expectations for straight-line towing test simulation. As a result of this work, it is decided to use k-ε turbulence model for the rest of the CFD simulations in this study.

First and second order upwind discretization methods are used for CFD calculations and solutions are converged after 1400 iterations. All of the runs have similar convergence history. Overall CPU time for a single run is 10.5 hours. Convergence history of k-ε turbulence model run at 10° angle of attack is given in Figure 4.13 as a sample:

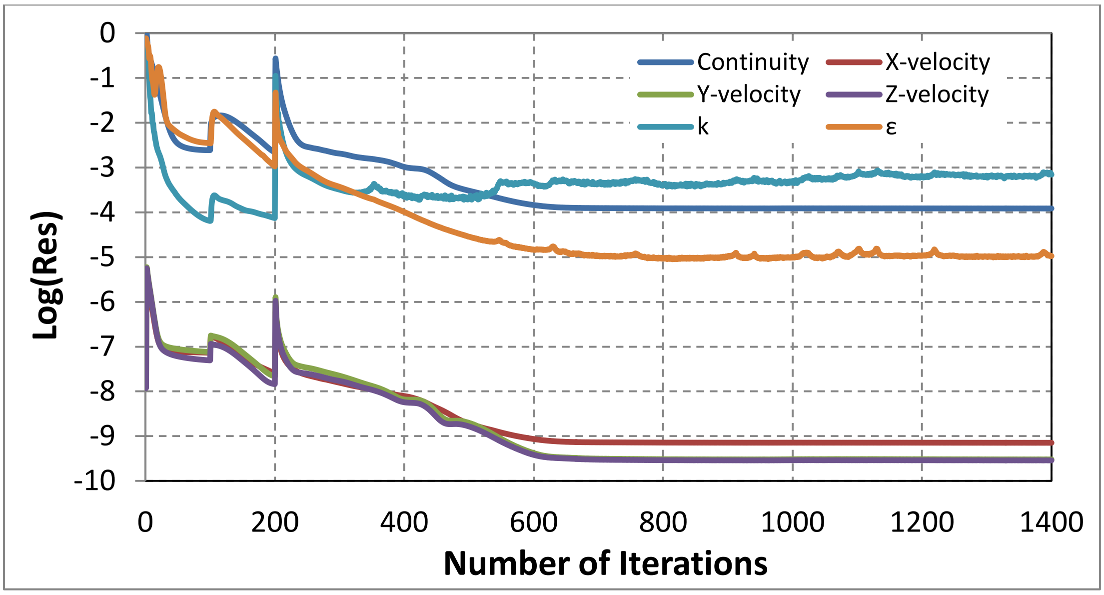

Figure 4.13 Convergence History of Steady Autosub Run (α=10°)

In addition flow field of the CFD run at α=10° is examined. Pressure distribution on the Autosub model and velocity distribution in flow domain are illustrated in Figure 4.14 and Figure 4.15:

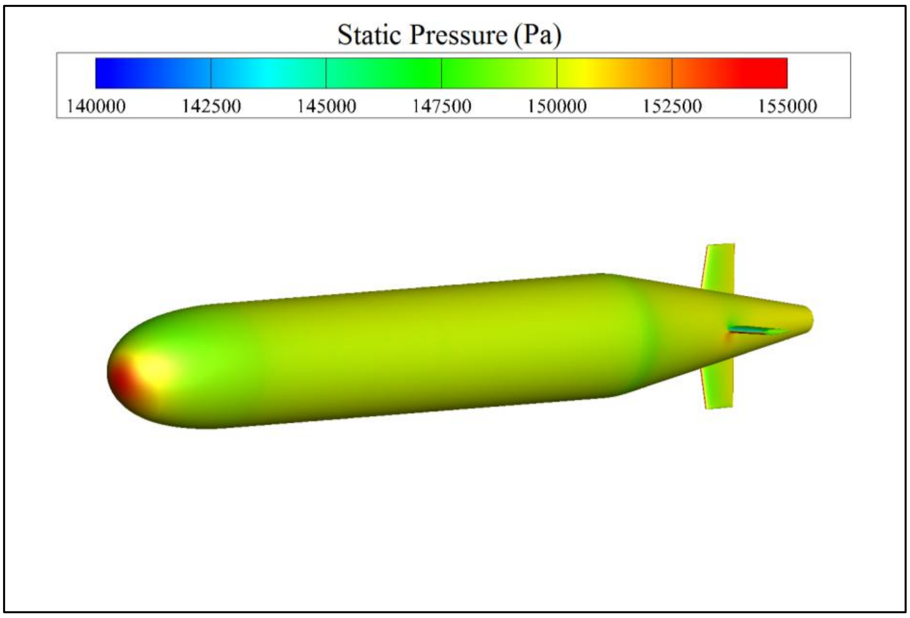

Figure 4.14 Pressure Distribution on Autosub Model according to Results of Towing Test Simulation (α=10°)

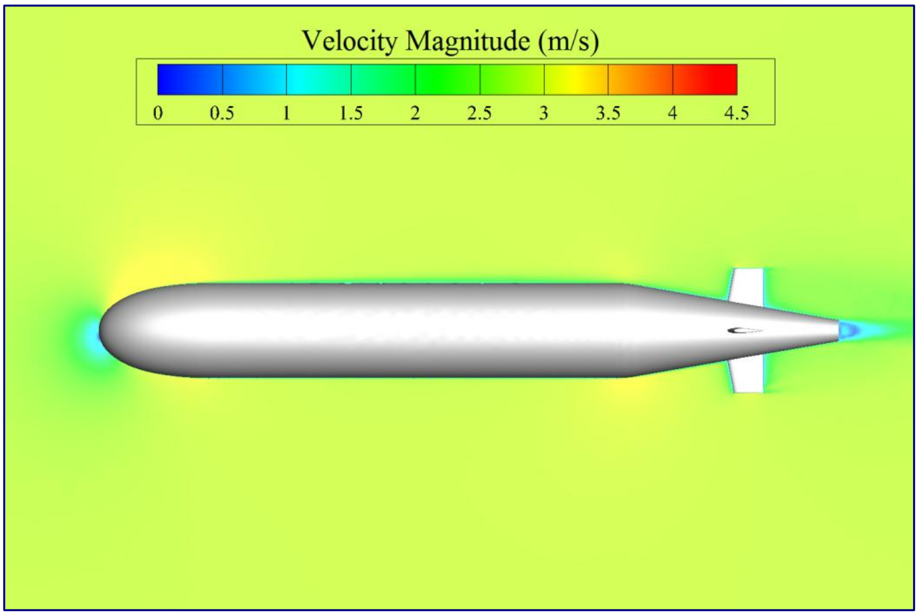

Figure 4.15 Velocity Distribution in Flow Domain according to Results of Autosub Towing Test Simulation (α=10°)

Pressure and velocity values are computed for given cruise conditions in Table 4.3.

4.2 DARPA Model Straight-line Towing Test Simulation

DARPA CFD simulations consist of same steps with Autosub simulations. Detailed information about CFD simulations of DARPA model will be given in this part.

4.2.1 Grid Generation

Grid generation of the DARPA model is similar to the Autosub model. Same strategy with the Autosub model is used and same grid element types which are given in Figure 4.2 are used. In addition cruise conditions of DARPA CFD simulations and DARPA model dimensions are similar with Autosub model. Since similar growth rates and element sizes are used for surface and volume grids, grid independence study is not repeated. Generated surface grid is shown in Figure 4.16:

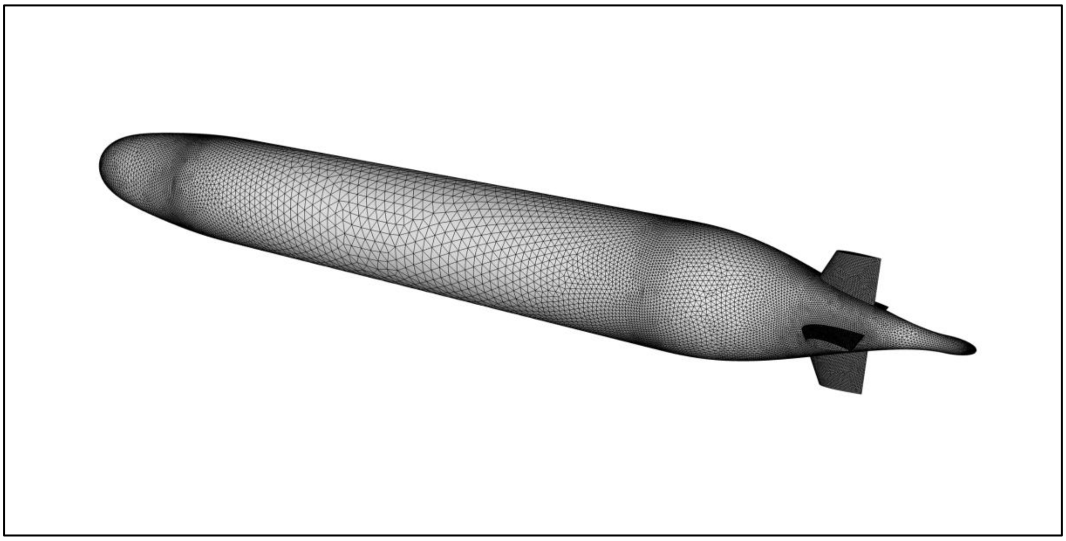

Figure 4.16 Surface Grid for DARPA Model

Boundary layer grid consists of 20 layers same as the Autosub model. First 10 of layers grow exponentially from first height and the other 10 layers grow to ensure that aspect ratio of last layer is %40. Generated boundary layer grid is shown in Figure 4.17:

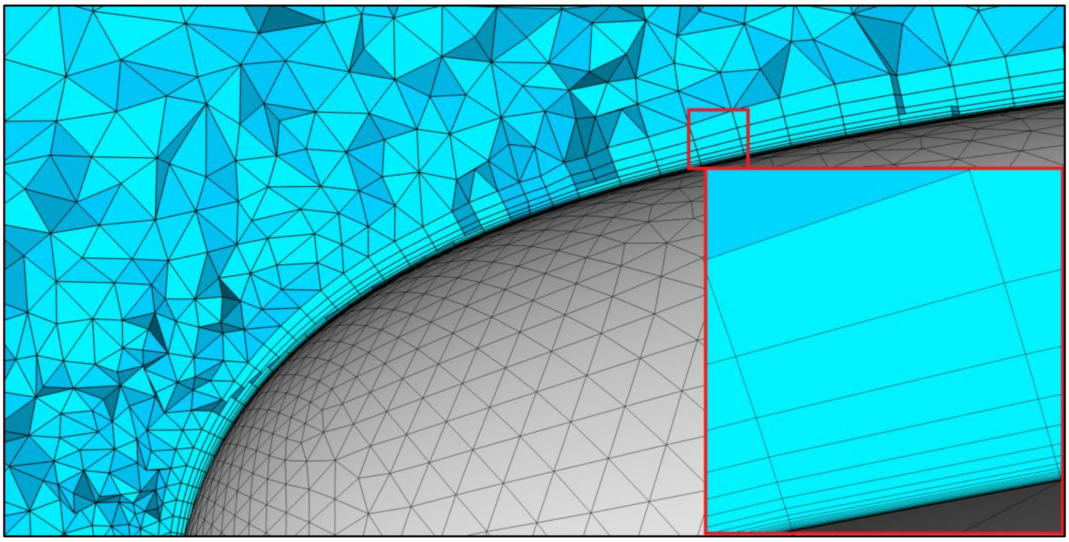

Figure 4.17 Boundary Layer Grid for DARPA Model

Similar to the Autosub model, volume grid is generated with linearly growing cell sizes from model surface to outer regions. Generated surface and volume grids are shown in Figure 4.18 and Figure 4.19:

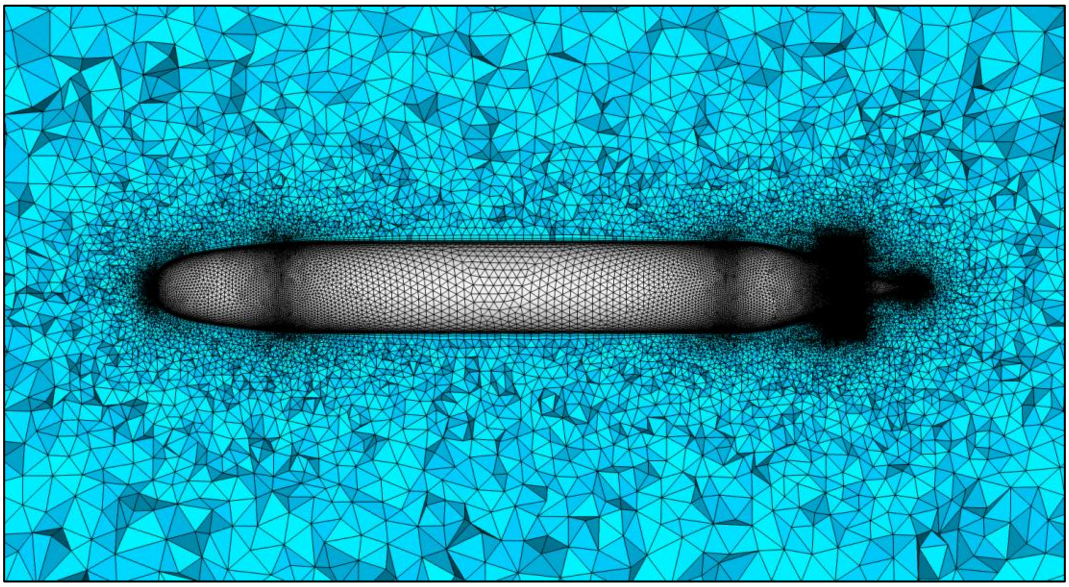

Figure 4.18 Surface and Volume Grids for DARPA Model

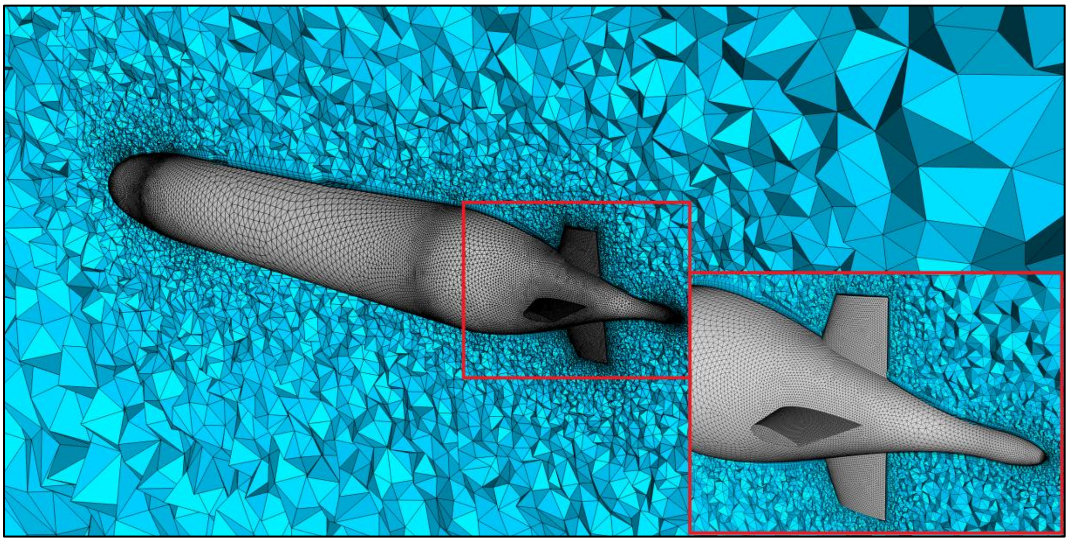

Figure 4.19 Volume and Detailed Tail Surfaces Grids for DARPA Moded

Element numbers of generated grid are given in Table 4.6:

Table 4.6 Element Numbers of DARPA Grid

Number of Surface Grid Elements	Number of Tetrahedron Elements	Number of Prism/Wedge Elements
67,580	1,351,600	2,029,865

Boundary layer methodology has been explained in section 4.1.1.2. First height value is calculated by Equation (4.4). To satisfy enhanced wall treatment approach, y^+ value that is in the viscous sublayer region is aimed according to the given relationship in Table 4.4.

Consistency of y^+ value is checked with pre-solution results. Results of y^+ values are given in Figure 4.20:

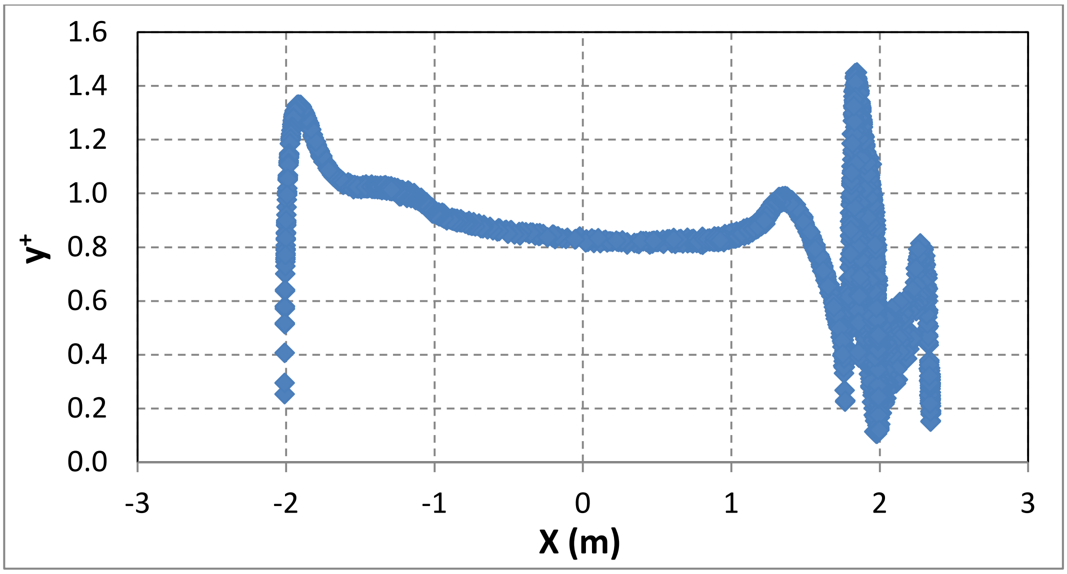

Figure 4.20 y^+ Values for DARPA Grid

Obtained y^+ values are below the aimed value at all points. Hence boundary layer grid is fine enough for DARPA Model CFD simulations.

4.2.2 Boundary Conditions

Same as the Autosub towing test simulations, the flow domain is defined large enough to minimize flow effects between model and boundaries. Also completely same boundary conditions are defined for flow domain as given in Figure 4.10.

4.2.3 CFD Simulation Results

DARPA straight-line towing test is simulated for cruise conditions given in Table 4.7. Cruise conditions are chosen according to experimental data. Steady-state CFD analyses are performed for chosen conditions and CFD results are compared with experimental data [12]. In addition, as a result of turbulence model selection study, k-ε turbulence model is used for CFD analyses.

Table 4.7 Cruise Conditions for DARPA Towing Test Simulations

Velocity (m/s)	3.34
Angle of Attacks (^{o})	0, 2, 4, 6, 8, 10, 12, 14, 16, 18
Ambient Pressure (Pa)	150,277

Computed X force coefficient results and experimental data are given with respect to angle of attack in Figure 4.21:

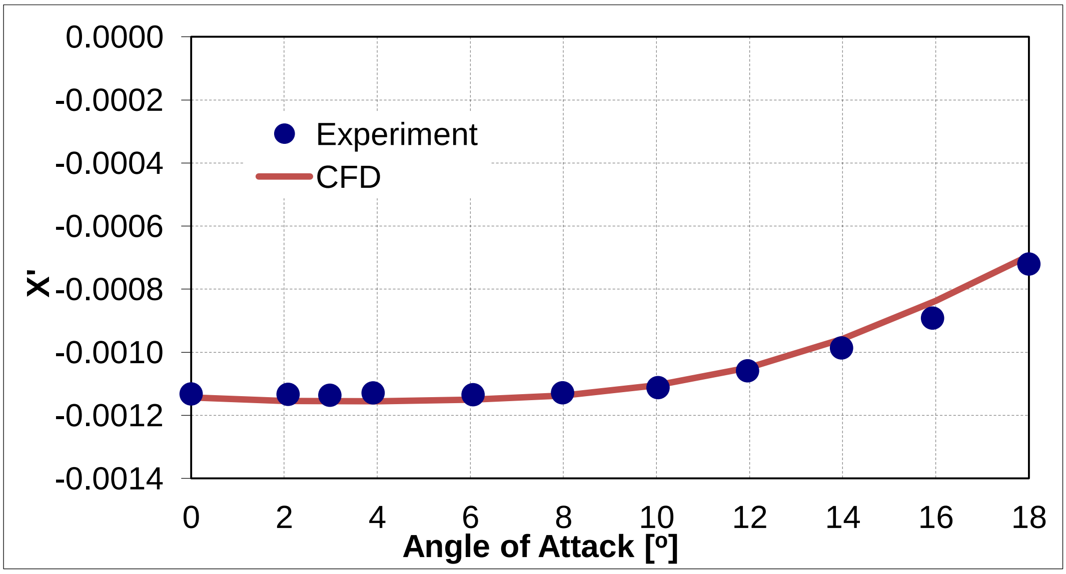

Figure 4.21 DARPA Model X Force Coefficient Results and Experimental Data With Respect to AOA [12]

Computed force and moment coefficients on Z direction and experimental data are given with respect to angle of attack in Figure 4.22 and Figure 4.23:

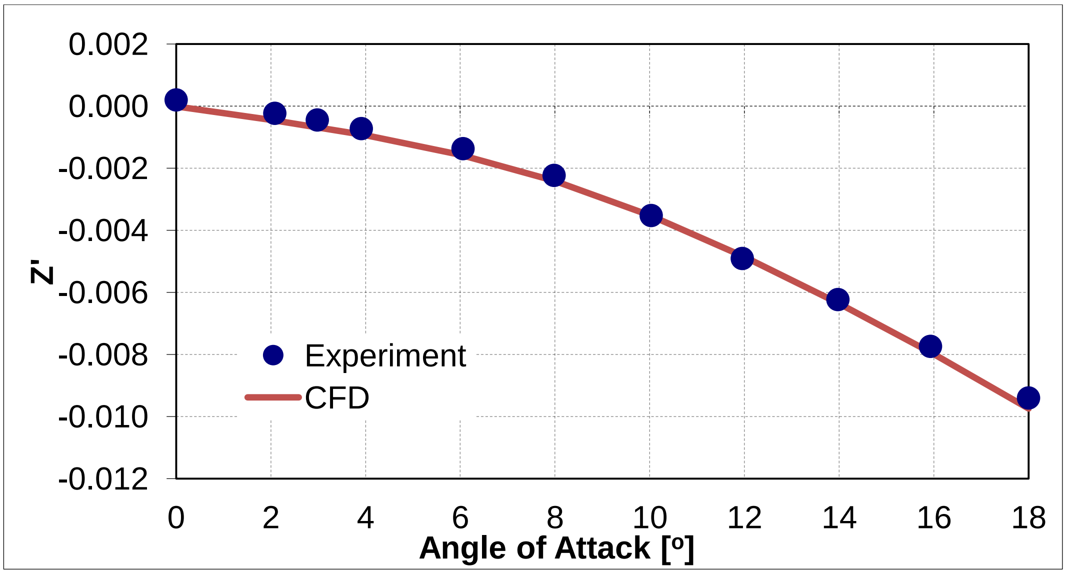

Figure 4.22 DARPA Model Z Force Coefficient Results and Experimental Data With Respect to AOA [12]

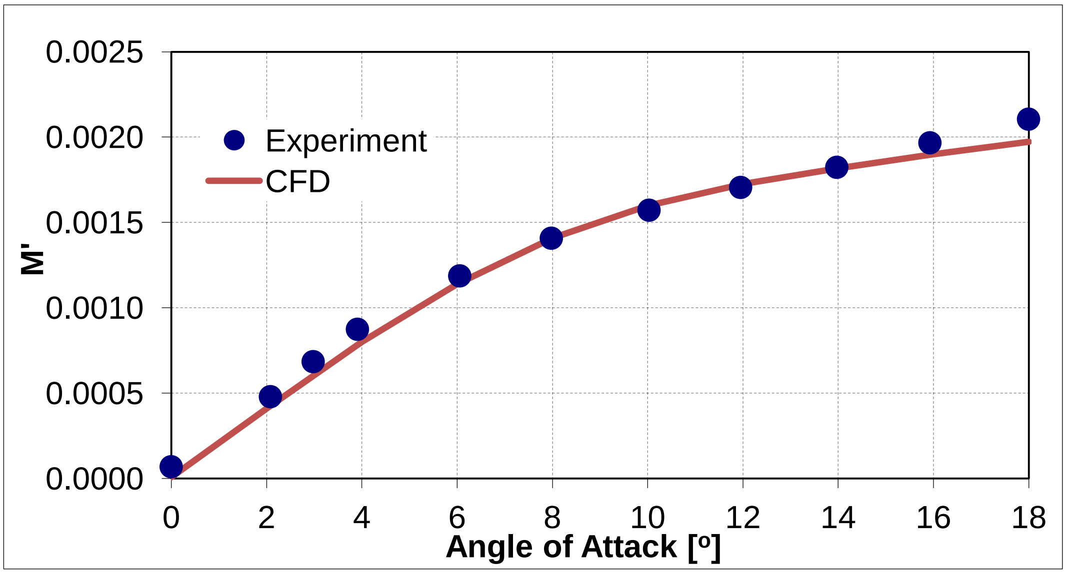

Figure 4.23 DARPA Model Pitch Moment Coefficient Results and Experimental Data With Respect to AOA [12]

As shown in figures, CFD results are in good agreement with experimental data. For an instance, CFD results at 18° angle of attack are examined and error percentages of comparisons between CFD results and experimental data are given in Table 4.8:

Table 4.8 Error Percentages of DARPA Towing Test Simulation Results (α=18°)

Coefficient	Error (%)
X'	3.60
Z'	3.59
M'	6.24

CFD results are very close to experimental data and maximum error is below 7%. These results satisfy expectations for DARPA straight-line towing test simulation.

First and second order upwind discretization methods are used for CFD calculations. 1900 iterations are needed for convergence. All of the runs have similar convergence history. Overall CPU time for a single run is 12.4 hours. Convergence history of run at 18° angle of attack is given in Figure 4.24:

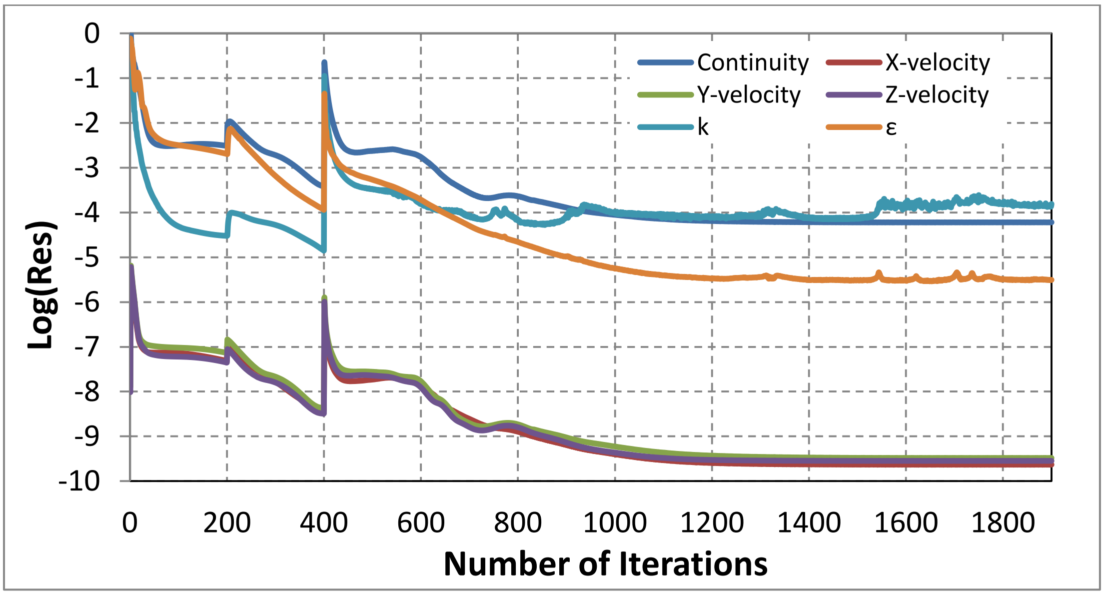

Figure 4.24 Convergence History of Steady DARPA Run (α=18°)

Flow field of the CFD run at α=18° is examined for towing test simulations. Pressure distribution on the DARPA model and velocity distribution in flow domain are illustrated in Figure 4.25 and Figure 4.26:

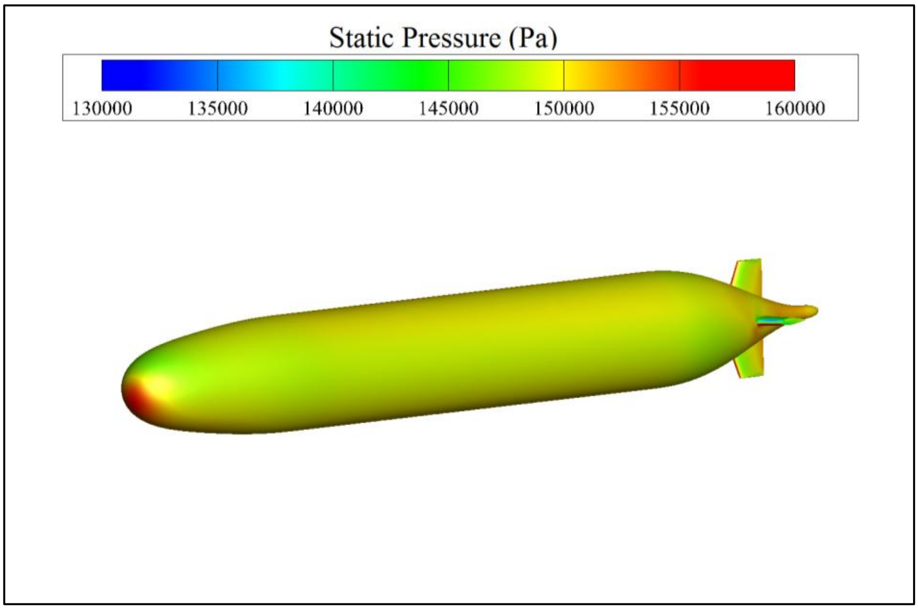

Figure 4.25 Pressure Distribution on DARPA Model according to Results of Towing Test Simulation (α=18°)

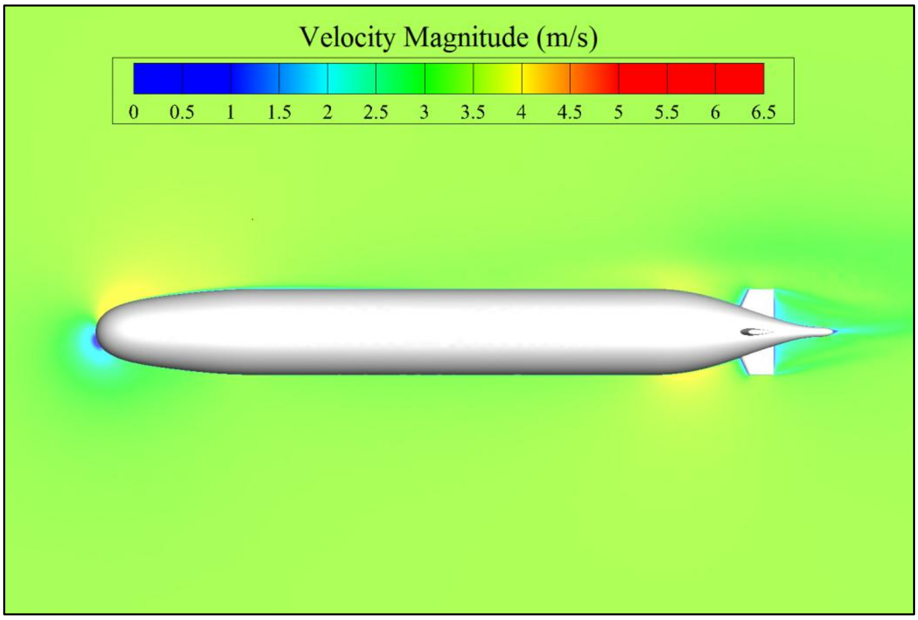

Figure 4.26 Velocity Distribution in Flow Domain according to Results of DARPA Towing Test Simulation (α=18°)

CHAPTER 5

SIMULATIONS OF ROTATING ARM TESTS

The Autosub test case model is used for RA test CFD simulations. RA CFD analyses are performed for constant angular velocity and for constant angular acceleration. In this part, detailed information about CFD modelling of RA tests and CFD analyses results will be given.

5.1 RA Test Simulation for Constant Angular Velocity

RA test CFD simulation process is completely same with straight-line towing test but flow domain is modeled differently as a semi-cylinder. Also different boundary and cell zone conditions are used to simulate RA test.

5.1.1 Grid Generation

The only difference between RA grid and towing test grid is shape of flow domain. Same surface and boundary layer grids are generated for Autosub model. Also cell sizes are grown with same rate. Since same surface and boundary layer grids with towing tests are used for RA tests, grid independence and boundary layer analysis studies are not repeated.

Surface and boundary layer grids are shown in Figure 4.6 and Figure 4.7 . In addition flow domain and volume grid are shown in Figure 5.1:

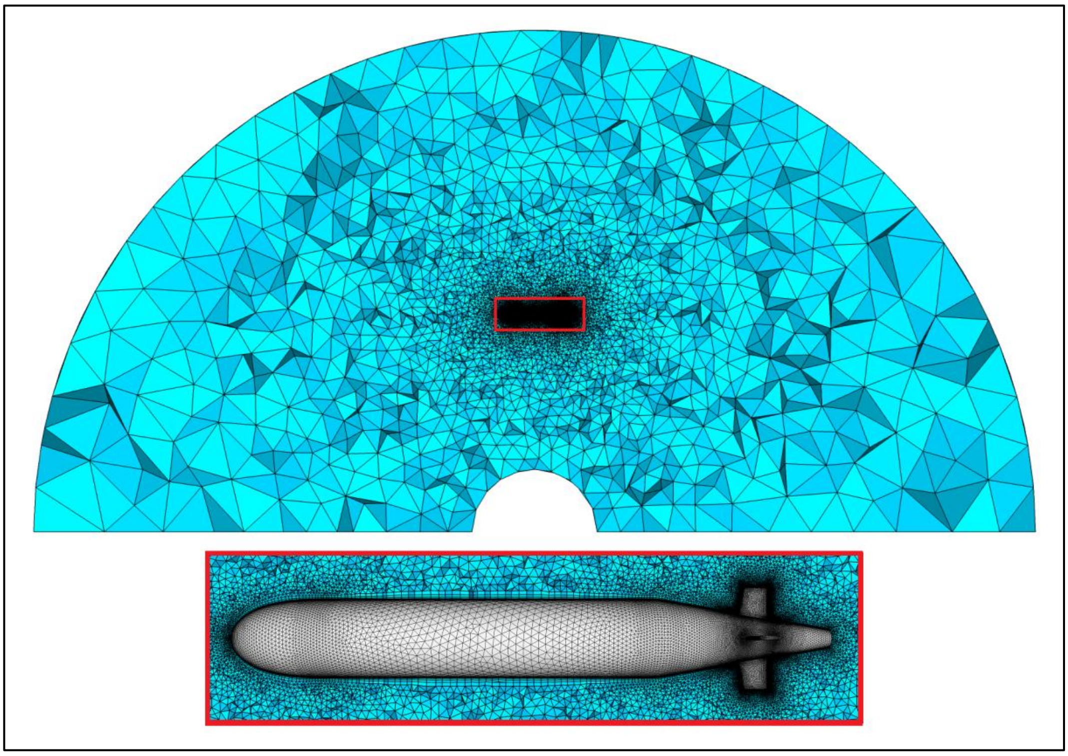

Figure 5.1 Flow Domain Grid for RA Test Simulations (Constant Velocity)

Element numbers of generated RA grid are given in Table 5.1:

Table 5.1 Element Numbers of RA Grid (Constant Velocity)

Number of Surface Grid Elements	Number of Tetrahedron Elements	Number of Prism/Wedge Elements
59,258	1,185,160	1,530,971

5.1.2 Boundary Conditions

Flow domain is defined as a semi-cylinder with a hole at the center. The radius of hole is equal to L, cylinder radius is equal to 8×L and height of cylinder is equal to 3×L. Then wall boundary condition is defined for the AUV model faces, symmetry boundary condition is defined for side faces, velocity inlet and pressure outlet boundary conditions are defined for lower flat faces. In addition moving reference frame cell zone condition is defined for entire domain. Flow domain and defined boundary conditions are illustrated in Figure 5.2:

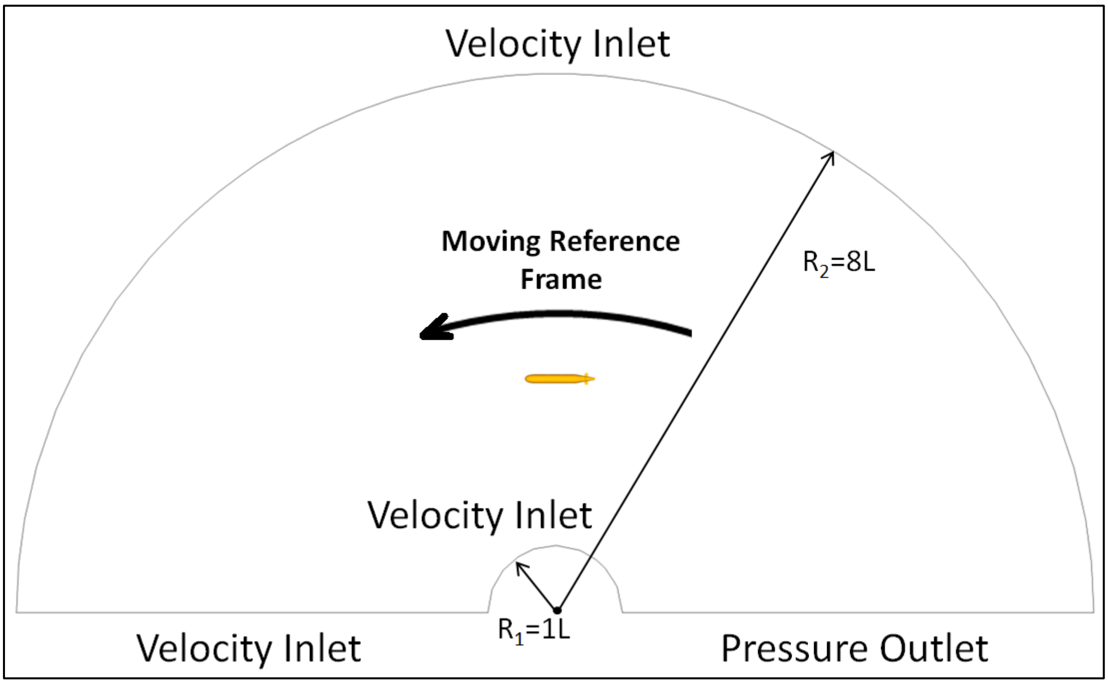

Figure 5.2 Flow Domain Boundary Conditions for Autosub RA Test Simulations (Constant Velocity)

5.1.3 CFD Simulation Results

Autosub RA test is simulated for cruise conditions given in Table 4.7. Cruise conditions are chosen according to experimental data. It is intended to obtain q dependent dynamic coefficients. Steady-state CFD analyses are performed for chosen conditions and CFD results are compared with experimental data [31].

Table 5.2 Cruise Conditions for Autosub RA Test Simulations

Turn Radius (R) (m)	13.0, 17.358, 26.0
Angular Velocity (q) (rad/s)	2.69/R
Ambient Pressure (Pa)	150,277

Where r' represents L/R, computed force and moment coefficients on the z direction are given with respect to r' in Figure 5.3 and Figure 5.4:

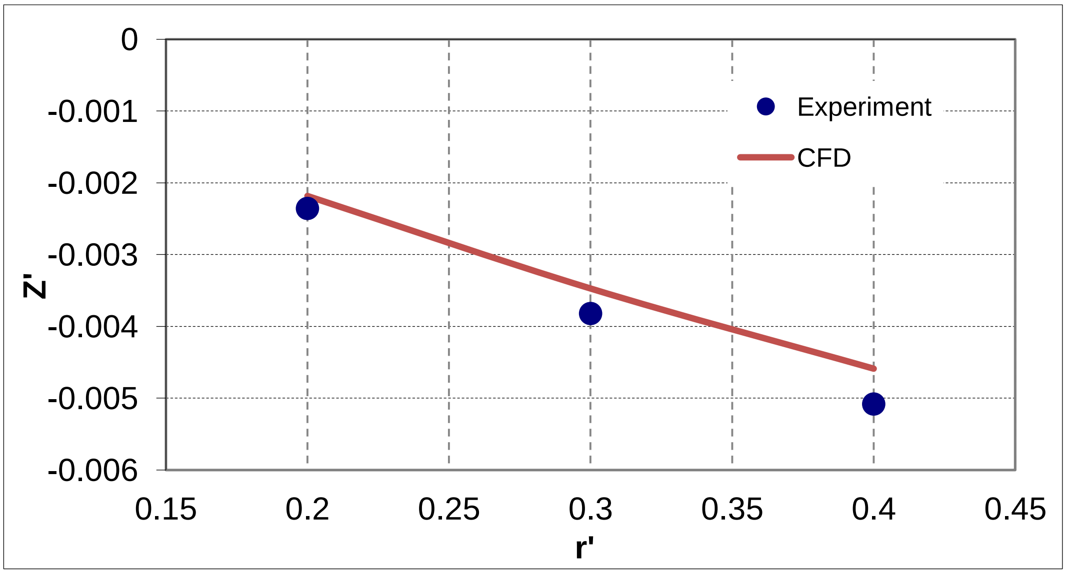

Figure 5.3 Z force coefficient With Respect to r' for Autosub RA Tests [31]

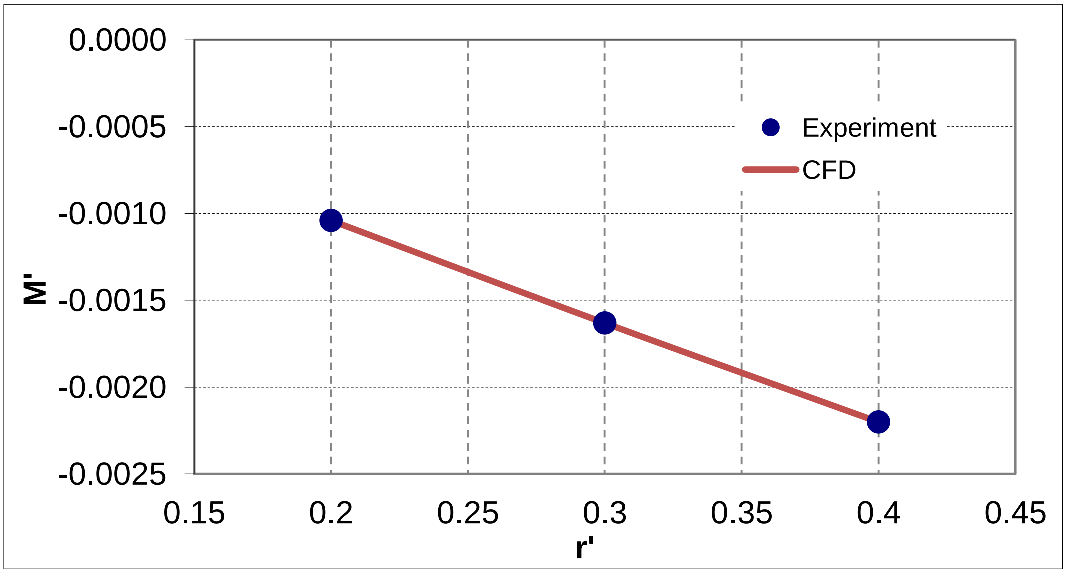

Figure 5.4 Pitch Moment Coefficient With Respect to r' for Autosub RA Tests [31]

As shown in figures, CFD results are in good agreement with experimental data. Also q dependent dynamic coefficients are calculated from these results and calculated coefficients are compared with experimental data. Calculation steps are given as follows:

Where

$$Z'_q = \frac{Z}{q\,{}^{1}/_{2}\,\rho V L^3} \tag{5.1}$$

$$Z' = \frac{Z}{{}^{1}/_{2}\,\rho V^2 L^2} \tag{5.2}$$

Then

$$Z'_q = \frac{Z'V}{qL} \tag{5.3}$$

The V can be written as

$$V = qR \tag{5.4}$$

Finally, relation between static and dynamic coefficients can be written as follows

$$Z'_q = \frac{Z'}{L/_R} = \frac{Z'}{r'} \tag{5.5}$$

According to this relation, Z'_q can be obtained from gradient of trend line of Z' results in Figure 5.3. Same strategy can be used for moment coefficients too. Calculated dynamic coefficients, reference CFD results and comparison with experimental data is given in Table 5.3:

Table 5.3 Calculated Dynamic Coefficients from Constant Angular Velocity RA Simulation and Experimental Data [4, 31]

Coefficient	CFD (x10^3)	Ref. CFD (x10^3)	Experiment (x10^3)	Error (%)
Z'_q	-12.02	-12.35	-12.64	4.9
M'_q	-5.80	-6.59	-5.35	8.4

Calculated dynamic coefficients are very close to the experimental data and errors are below 10%. Results satisfy expectations from RA test CFD simulation for dynamic coefficients.

In addition first and second order upwind discretization methods are used for CFD calculations. 3400 iterations are needed for convergence. All of the runs have similar convergence history and overall CPU time for a single run is 23.6 hours. Convergence history of 17.358 m turn radius CFD analysis is given in Figure 5.5:

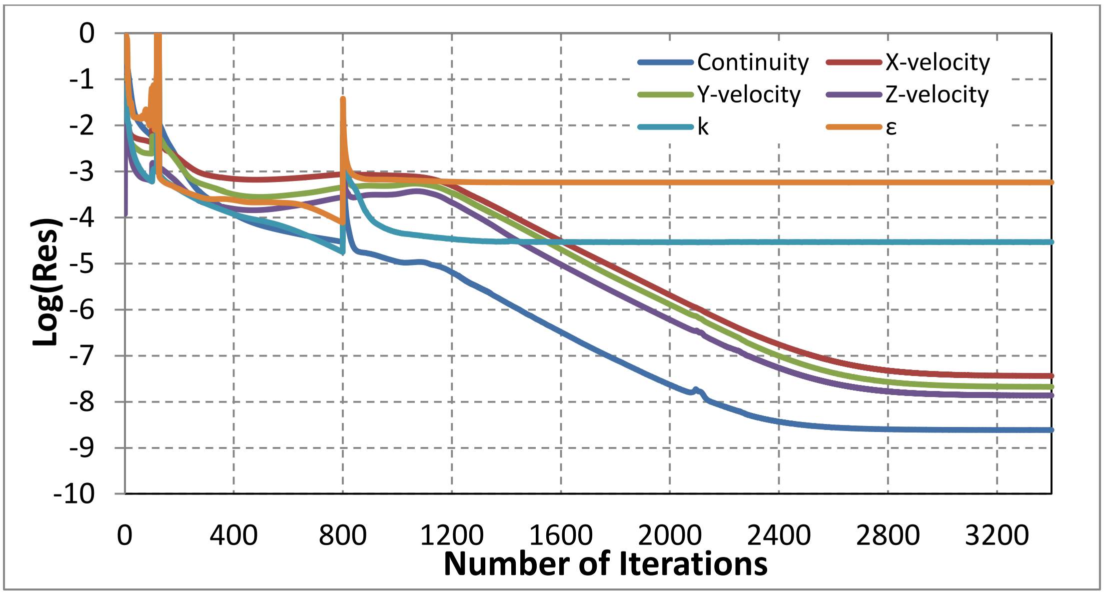

Figure 5.5 Convergence History of Steady RA Analysis (R=17.358 m)

Flow field for turn radius 17.358 m is examined as a sample result. Pressure distribution on the Autosub model and velocity distribution in the flow domain are shown in Figure 5.6 and Figure 5.7:

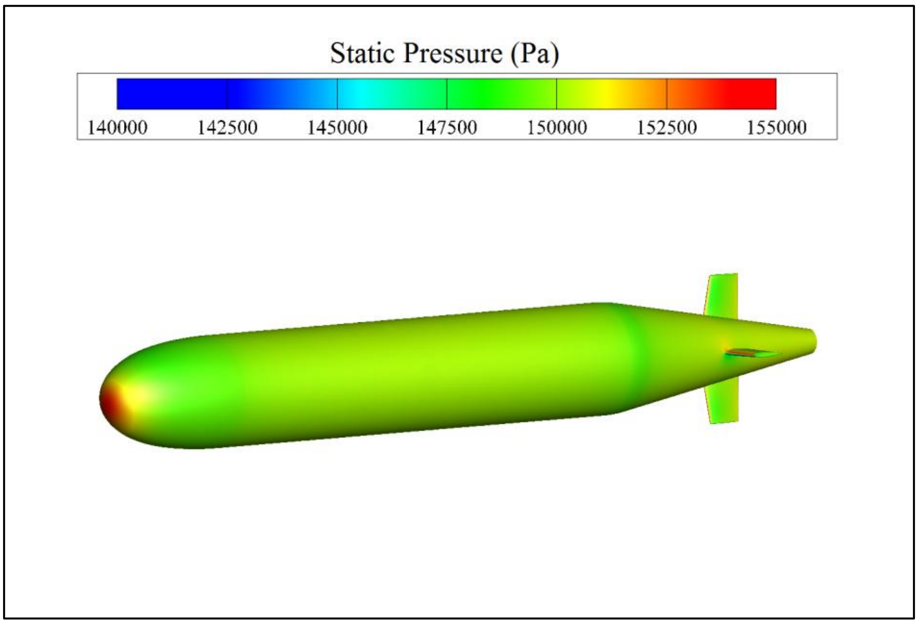

Figure 5.6 Pressure Distribution on Autosub Model according to Results of RA Test Simulation (R=17.358 m)

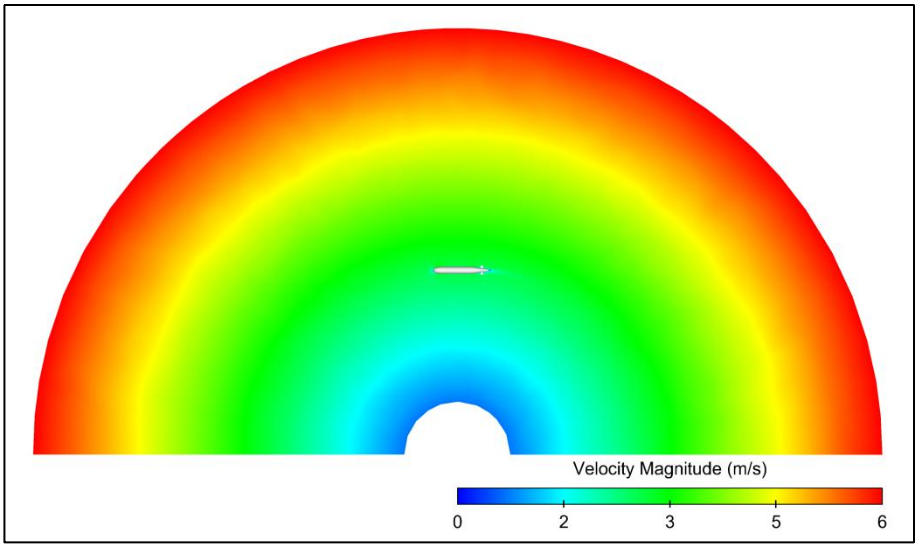

Figure 5.7 Velocity Distribution in Flow Domain according to Results of RA Test Simulation (R=17.358 m)

Velocity vectors in flow domain are also shown in Figure 5.8:

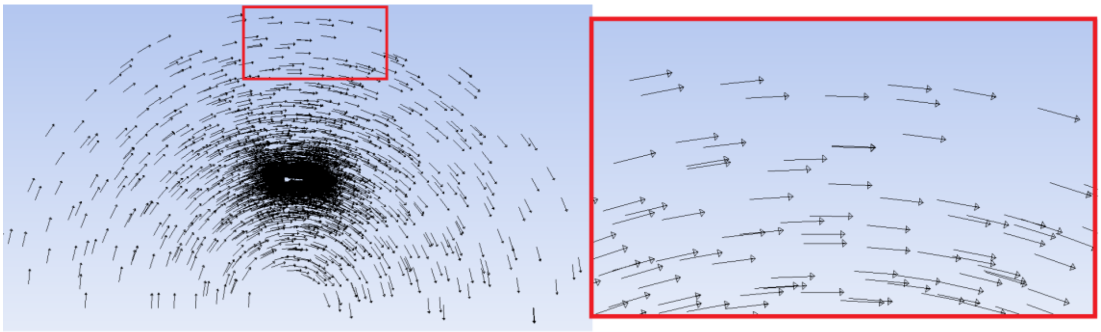

Figure 5.8 Velocity Vectors in Flow Domain according to Results of RA Test Simulation (R=17.358 m)

5.2 RA Test Simulation for Constant Angular Acceleration

CFD modelling of a RA simulation for angular acceleration has several differences. First of all, process is time dependent hence transient solution is needed and two sub-domains are used to define accelerated motion. In addition different shaped flow domain is used to keep distance between model and inlet boundary because inner domain moves inside of the outer domain with a radial path. Detailed information about RA test simulation for constant angular acceleration will be given in this part.

5.2.1 Grid Generation

Differences between two RA grids are shape of flow domain and sub-domains. On the other hand, same surface and boundary layer grids are used for model. Also cell sizes are grown with same rate. Surface and boundary layer grids are shown in Figure 4.6 and Figure 4.7. Flow domain and volume grid are shown in Figure 5.9:

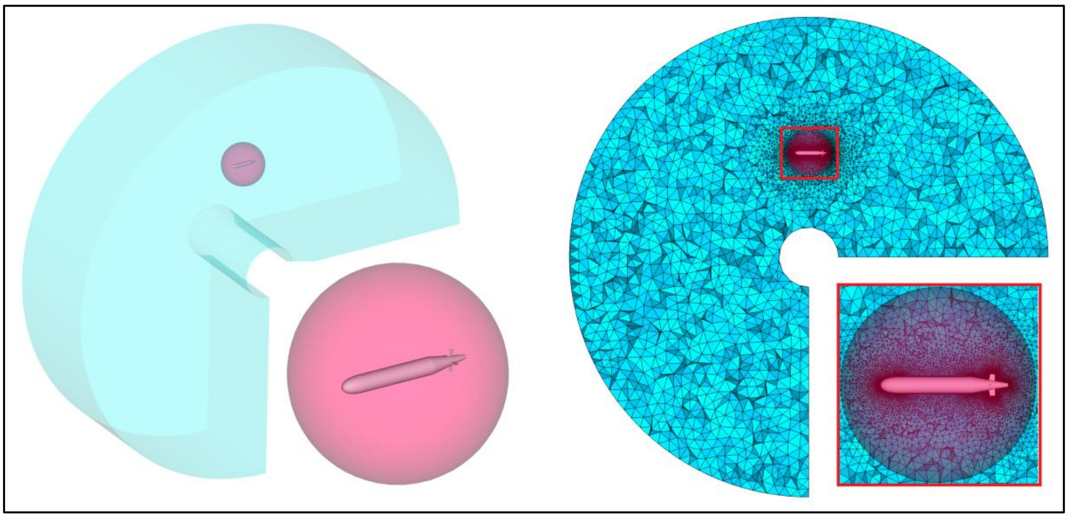

Figure 5.9 Flow Domain and Volume Grid for RA Test Simulation (Constant Acceleration)

Inner domain moves inside of the outer domain hence outer domain grid changes with respect to time. Volume grids at t= 0s and t=3s are shown in Figure 5.10:

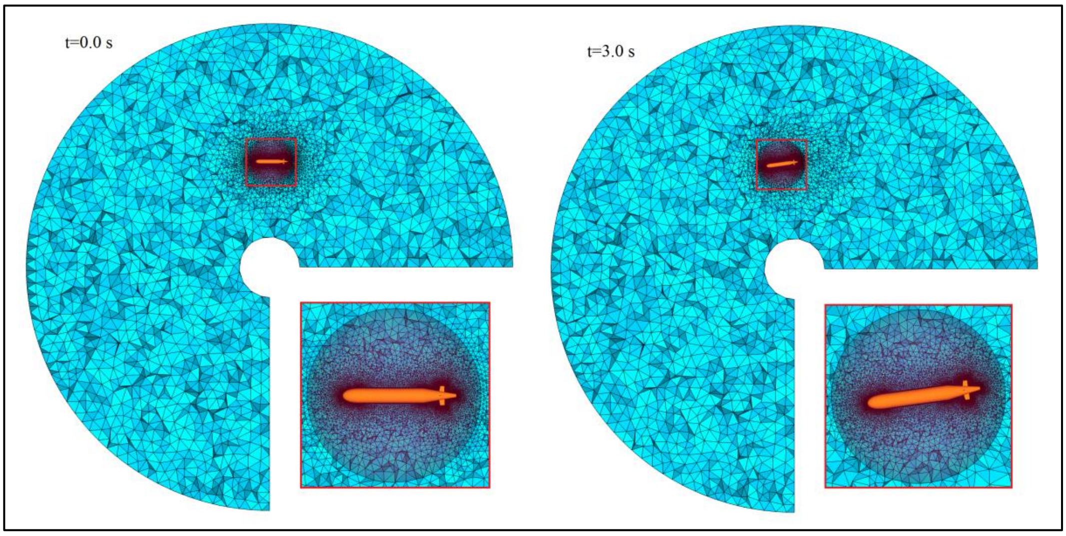

Figure 5.10 Volume Grids at t=0 s and t=3 s for RA Test Simulation (Constant Acceleration)

Element numbers of generated RA grid are given in Table 5.4:

Table 5.4 Element Numbers of RA Grid (Constant Acceleration)

Number of Surface Grid Elements	Number of Tetrahedron Elements	Number of Prism/Wedge Elements
59,258	1,185,160	1,712,402

5.2.2 Boundary Conditions

Flow domain is similar to the constant velocity RA grid and defined boundary conditions are similar too. Except the face which separates sub-domains, all of the other boundary conditions are same and interface boundary condition is defined for this face. Also while moving reference frame cell zone condition is defined for inner and outer domain, mesh motion is defined for only inner domain. Flow domain and defined boundary conditions are illustrated in Figure 5.11:

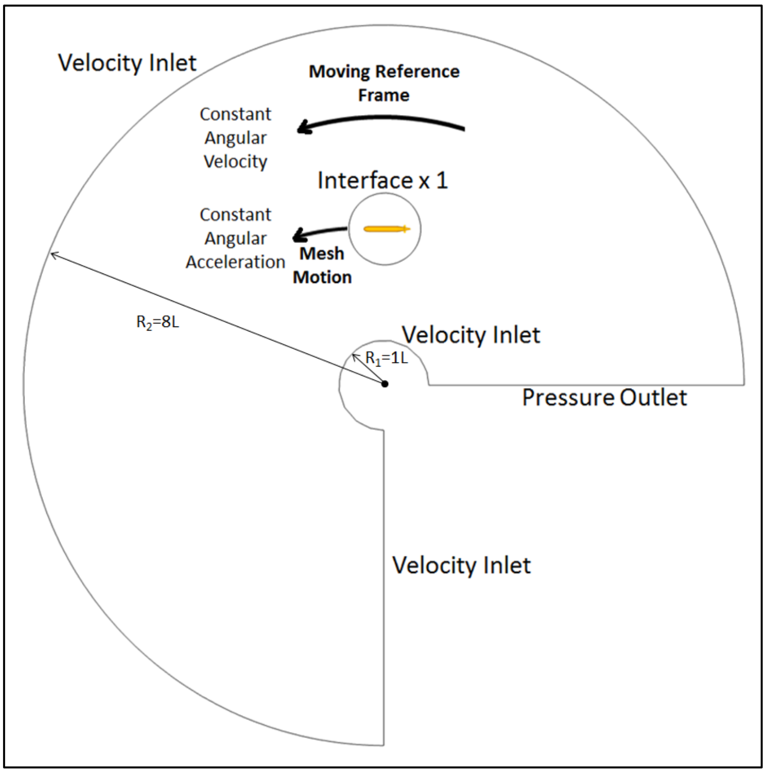

Figure 5.11 Flow Domain Boundary Conditions for RA Test Simulations (Constant Acceleration)

5.2.3 CFD Simulation Results

Autosub RA test with acceleration is simulated for only 17.358 m turn radius. Initial angular velocity is 0.1 rad/s and it reaches 0.19 rad/s value with 0.03 rad/s^2 angular acceleration. Transient CFD analysis is performed for given conditions and it is intended to obtain $\dot{q}$ dependent dynamic coefficients. These coefficients are called as added mass and added inertia derivatives and occur due to acceleration. The following equations are used for calculation of $\dot{q}$ dependent coefficients [34].

$$Z_t - Z_s = I_{a-m}\dot{q} \qquad M_t - M_s = I_{a-i}\dot{q} \tag{5.6}$$

And

$$Z'_{\dot{q}} = \frac{I_{a-m}}{{}^1\!/_2\,\rho L^4} \qquad M'_{\dot{q}} = \frac{I_{a-i}}{{}^1\!/_2\,\rho L^5} \tag{5.7}$$

Transient and steady forces on the z direction are represented by Z_t and Z_s and transient and steady pitch moment results are represented by M_t and M_s. I_{a-m} and I_{a-i} represents added mass and added inertia terms. Steady force and moment results are obtained from constant velocity RA simulation for 17.358 turn radius. Steady and Transient force and moment results are given in Figure 5.12 and Figure 5.13:

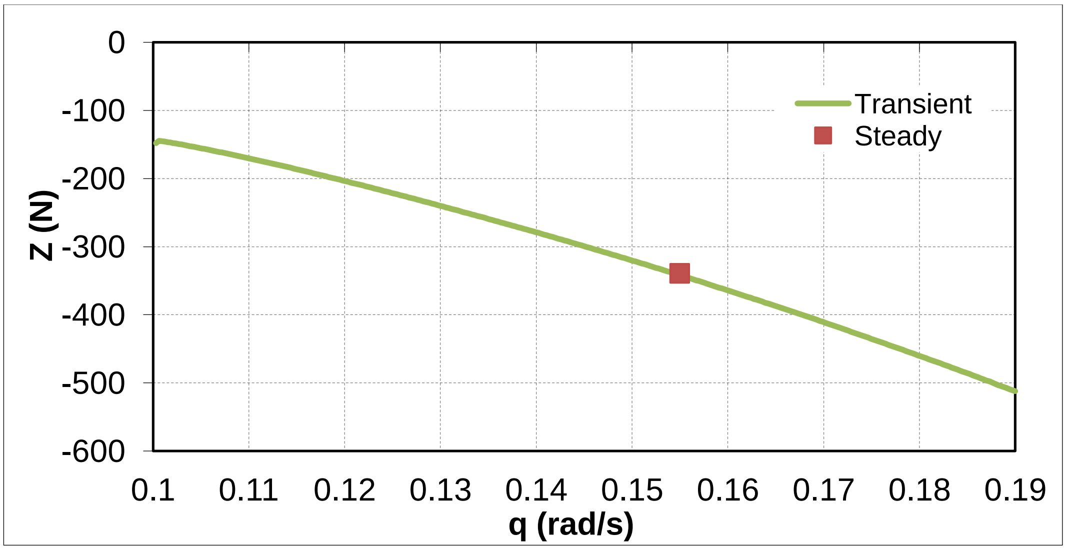

Figure 5.12 RA Test Simulation Transient and Steady Z Force Results (R=17.358 m)

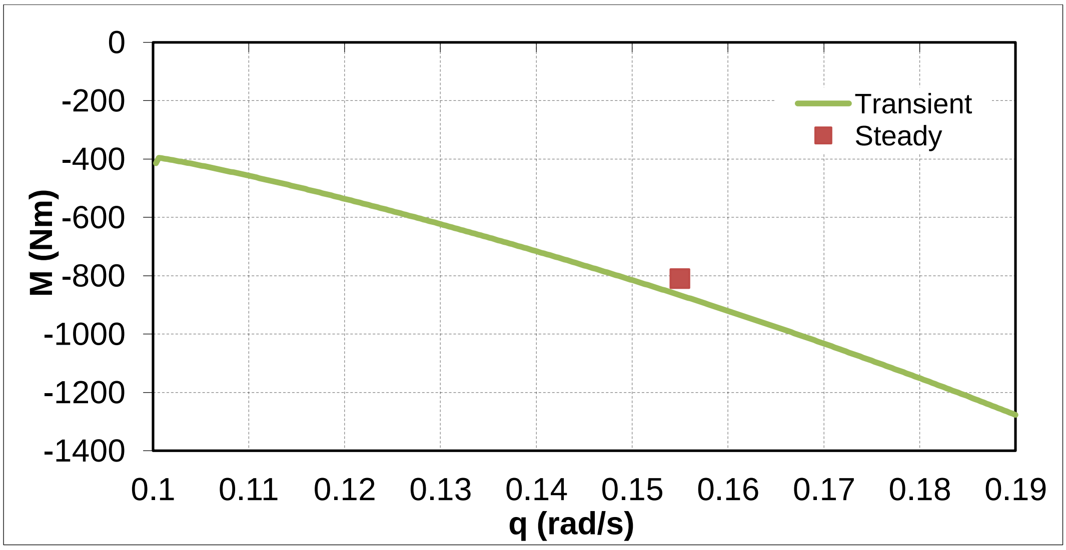

Figure 5.13 RA Test Simulation Transient and Steady Pitch Moment Values (R=17.358 m)

Dynamic coefficients are calculated by using Equations (5.6) and (5.7). Calculated $\dot{q}$ dependent coefficients and experimental data are given in Table 5.5 [13]:

Table 5.5 Calculated Dynamic Coefficients from Constant Acceleration RA Simulation and Experimental Data [13]

Coefficient	CFD (x10^3)	Experiment (x10^3)	Error (%)
$Z'_{\dot{q}}$	-0.1972	-0.1691	16.6
$M'_{\dot{q}}$	-0.9798	-0.9801	0.1

Calculated $M'_{\dot{q}}$ coefficient is very close to the experimental data and error is 0.1%. On the other hand, calculated $Z'_{\dot{q}}$ is close to the experimental data but error is 16.6%. Occurrence of greater error can be explained by that force derivate is smaller than moment derivative and smaller values cause larger errors. Results satisfy expectations from CFD simulations and this CFD modelling technique can be used for design processes.

In addition CFD analysis is initialized as a steady analysis and similar to the constant velocity RA analysis, MRF cell zone condition is defined for entire flow domain. Converged data file of steady analysis is used as start point and transient CFD analysis is continued on this data file to make convergence easy. Time step is selected as 0.01s and 50 sub-iterations are done for transient CFD analysis. Overall CPU time is 7.5 days.

Besides flow field is examined and pressure distribution on the Autosub model and is shown in Figure 5.14:

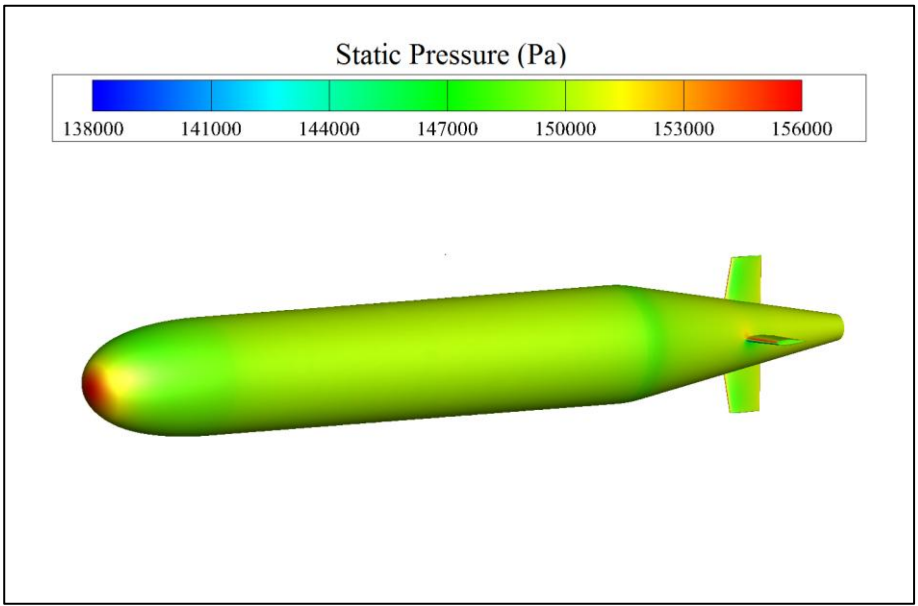

Figure 5.14 Pressure Distribution on Autosub Model at 3rd s (R=17.358 m)

CHAPTER 6

SIMULATIONS OF PLANAR MOTION MECHANISM TESTS

The Autosub test case model is used for PMM test CFD simulations. CFD analyses are performed for pure heave motion and combined motion of PMM. In this part, detailed information about CFD modelling of PMM tests and CFD analyses results will be given.

6.1 Pure Heave Motion Simulation

PMM pure heave motion CFD simulation process is completely same with the other test simulations. Flow domain is modeled similar to the towing test simulations but consists of two sub-domains; inner domain and outer domain. Also same boundary conditions are used for boundary faces except the interface between sub-domains.

6.1.1 Grid Generation

PMM grids are generated similar with towing test grids. Same model surface and boundary layer grids are used. Also cell sizes are grown with same rate. The PMM grids are consist of sub-domains and an interface separates these sub-domains. That is the only difference between PMM grids and towing test grids. Surface and boundary layer grids are shown in Figure 4.6 and Figure 4.7 and flow domain and volume grid are shown in Figure 6.1:

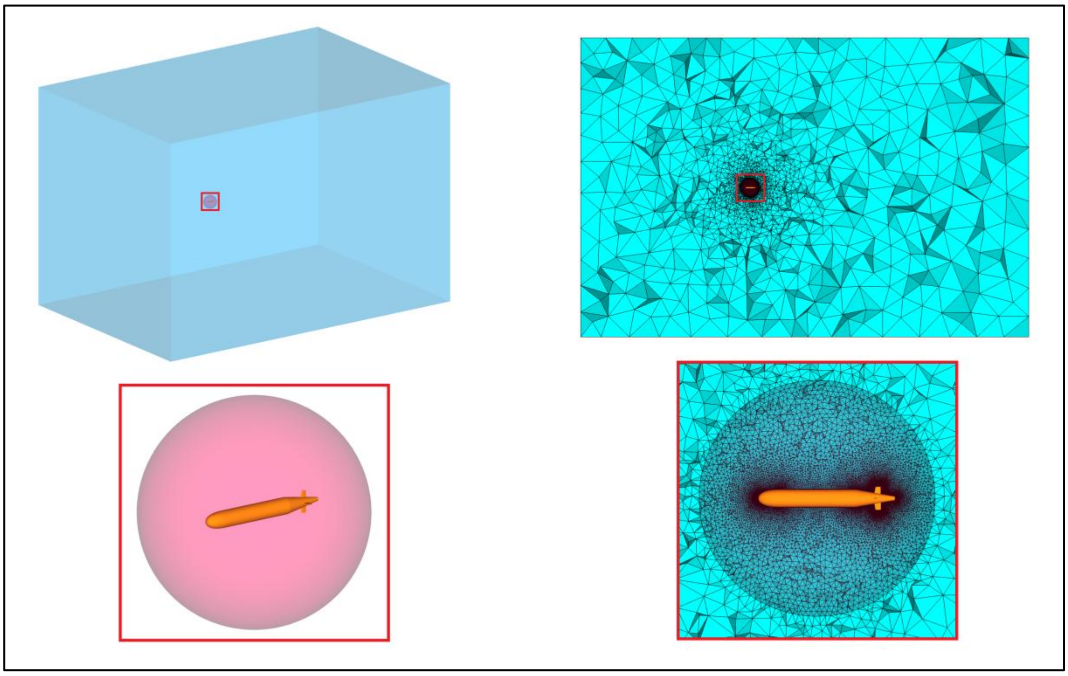

Figure 6.1 Flow Domain and Volume Grid for Pure Heave Test

In addition inner domain moves inside of the outer domain hence outer domain grid changes by time. Change of volume grid with respect to time is illustrated in Figure 6.2:

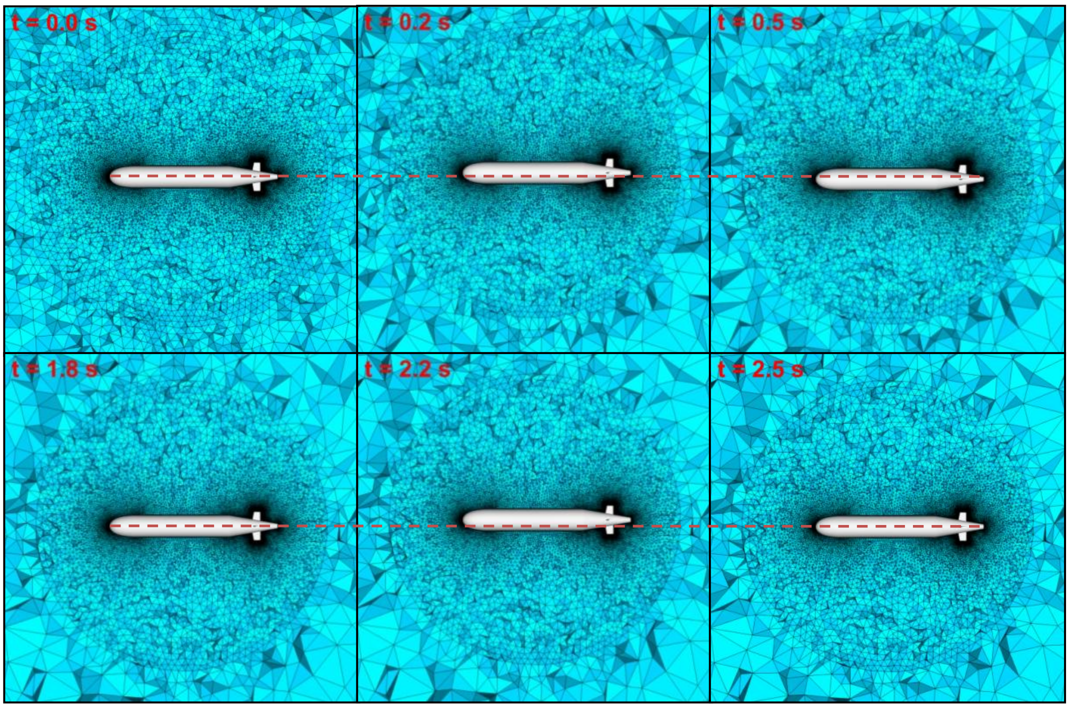

Figure 6.2 Change of Volume Grid With Respect to Time for Pure Heave Motion Simulation

6.1.2 Boundary Conditions

Flow domain grid and boundary conditions are similar to the straight-line towing test. Except the face which separates sub-domains, all of the other boundary conditions are same and interface boundary condition is defined for this face. In addition deformable dynamic mesh is defined for inner domain and mesh motion is defined by using FLUENT “user defined function”. Velocity inlet BC is defined for front and lower faces, pressure outlet BC is defined for back and upper faces and symmetry BC is defined for side faces. Flow domain and defined boundary conditions are illustrated in Figure 6.3:

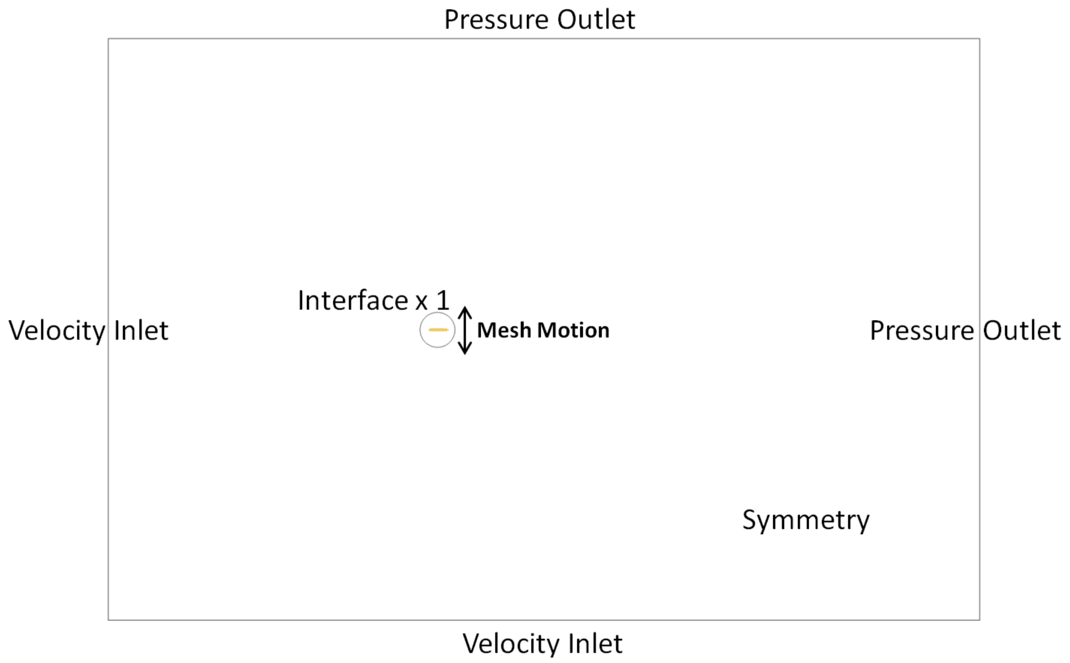

Figure 6.3 Flow Domain and Defined BCs for Pure Heave Motion

6.1.3 CFD Simulation Results

Pure heave motion is simulated for Autosub model. Transient CFD analysis is performed for given cruise conditions in Table 6.1 and it is intended to obtain w and $\dot{w}$ dependent dynamic coefficients.

Table 6.1 Cruise Conditions for Pure Heave Motion Simulation

Free Stream Velocity (m/s)	2.69
Amplitude (m)	0.1
Frequency (Hz)	1.5
Ambient Pressure (Pa)	150277.0

Pure heave motion is defined with a sinusoidal function by using an UDF file. Sinusoidal function is given by Equation (6.1):

$$2\pi a f \times \cos(2\pi f t) \qquad (6.1)$$

Time dependent force and moment coefficients on the z direction are obtained from CFD simulation and results are compared with experimental data [13]. Results are given in Figure 6.4 and Figure 6.5:

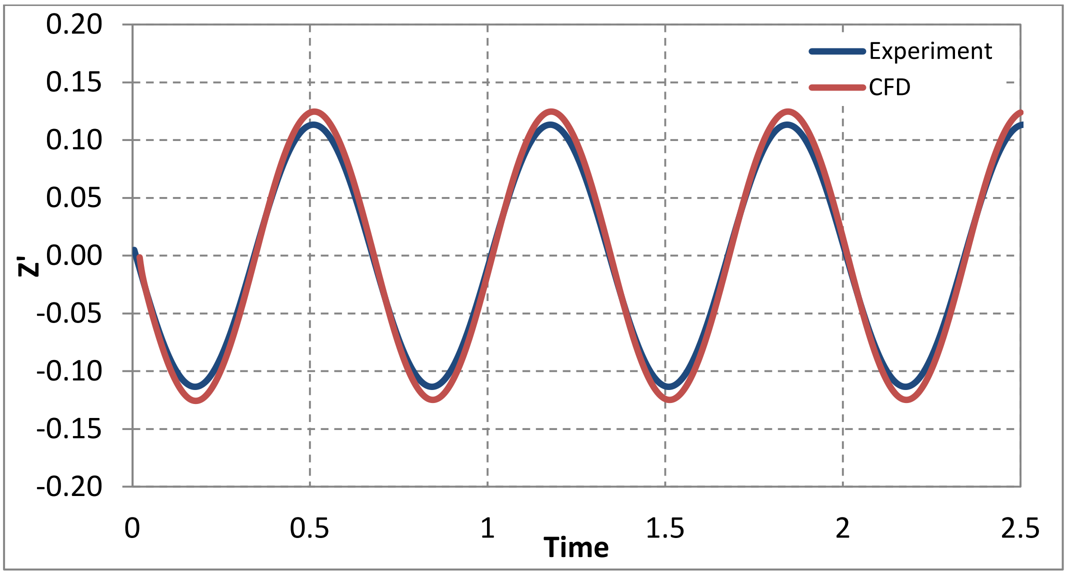

Figure 6.4 Z Force Coefficient With Respect to Time for Pure Heave Motion Simulation [13]

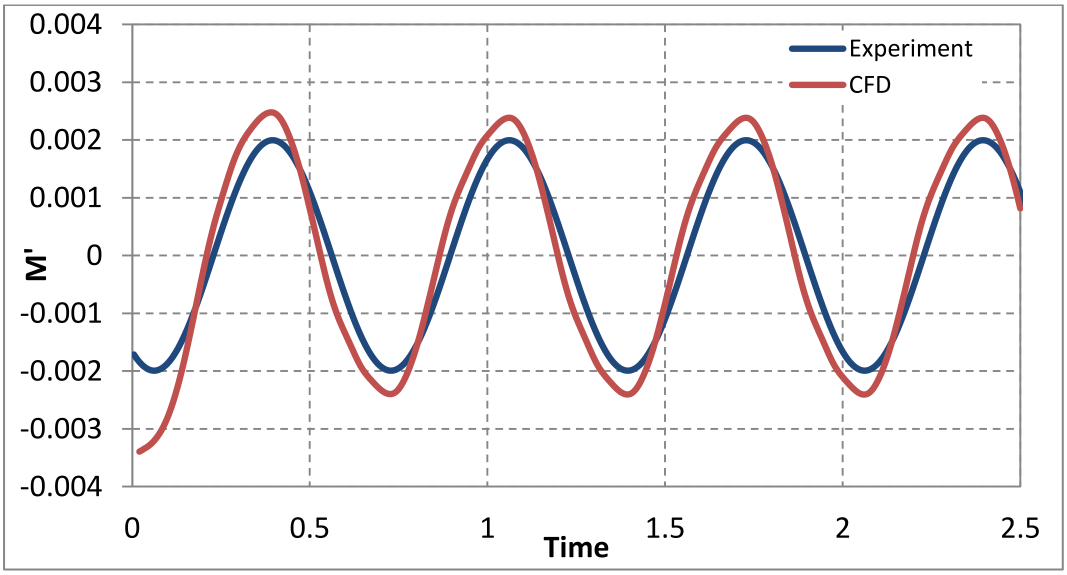

Figure 6.5 Pitch Moment Coefficient With Respect to Time for Pure Heave Motion Simulation [13]

It must be noted that experimental data in figures are obtained from experimental results of dynamic coefficients by using following equations of motion [13]:

$$Z'(t) = Z'_w \cdot w' + Z'_{\dot{w}} \cdot \dot{w}' + Z'_q \cdot q' + Z'_{\dot{q}} \cdot \dot{q}' \qquad (6.2)$$

$$M'(t) = M'_w \cdot w' + M'_{\dot{w}} \cdot \dot{w}' + M'_q \cdot q' + M'_{\dot{q}} \cdot \dot{q}' \qquad (6.3)$$

Pure heave motion does not include q and $\dot{q}$ terms therefore these terms are ignored for pure heave calculations. Beside these equations of motion are used in two regression analyses to obtain dynamic derivatives from time dependent CFD results. The regression analyses are performed by using MINITAB commercial program. Obtained dynamic coefficients, reference CFD results and experimental data are given in Table 6.2:

Table 6.2 Calculated Dynamic Coefficients from Pure Heave Simulation and Experimental Data [13, 18]

Coefficient	CFD ($x10^3$)	Ref. CFD ($x10^3$)	Experiment ($x10^3$)	Error (%)
Z'_w	-33.81	-32.0	-29.13	16.0
M'_w	5.57	6.1	4.68	25.5
$Z'_{\dot{w}}$	-19.29	-19.0	-17.39	10.9
$M'_{\dot{w}}$	-0.18	-0.16	-0.17	4.67

Maximum error is 25.5% and belongs to M'_w result. Error percentages seem to be higher compared to the previous simulation results but pure heave motion is more complex than the previous ones for CFD modelling. This complexity can be shown as the source of increasing error percentages. Also it is known that results of two different hydrodynamic tests can be varied for such a complex motion. In conclusion results are in good agreement with experimental data. Results satisfy expectations and this CFD modelling can be used in preliminary and conceptual design processes.

In addition similar to the RA with constant angular acceleration analysis, CFD analysis is initialized as a steady analysis and after convergence of steady run, transient CFD analysis is continued on steady CFD analysis data file to make convergence easy. Time step is selected as 0.005 s and 30 sub-iterations are done for transient CFD analysis. Overall CPU time is 9.8 days.

Besides flow field is examined and velocity distribution with respect to time is shown in Figure 6.6:

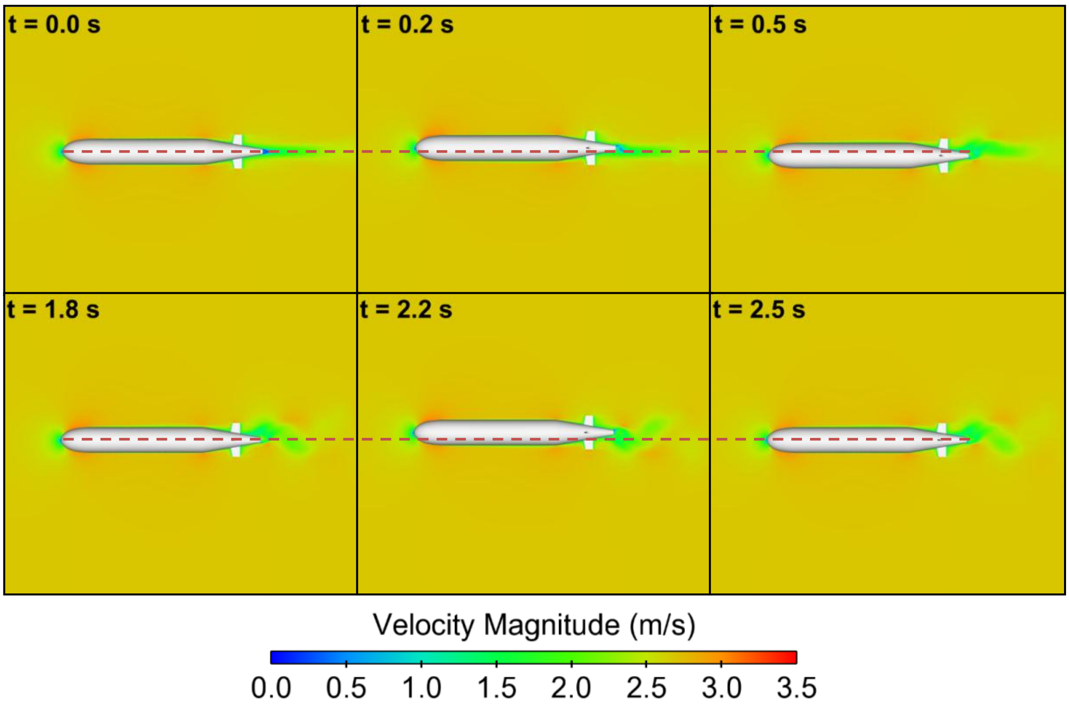

Figure 6.6 Velocity Distribution With Respect to Time for Pure Heave Motion Simulation

6.2 Combined Motion Simulation

PMM combined motion CFD simulation process is completely same with the other test simulations and flow domain is same with the pure heave domain. In addition same boundary conditions with pure heave simulation are defined for boundary faces.

6.2.1 Grid Generation

The only difference between pure heave and combined motion grids is number interfaces. There are two interfaces in combined motion grid, one of them belongs to outer domain and the other one belongs to inner domain. But there is only one interface in pure heave motion grid and it defines boundaries for both of the sub-domains. Since same grids with previous analyses are used detailed visuals are not shown again. Surface grid is shown in Figure 4.6, boundary layer grid is shown in Figure 4.7, flow domain and volume grid are shown in Figure 6.1. In addition volume grid changes with respect to time. This change is shown in Figure 6.7:

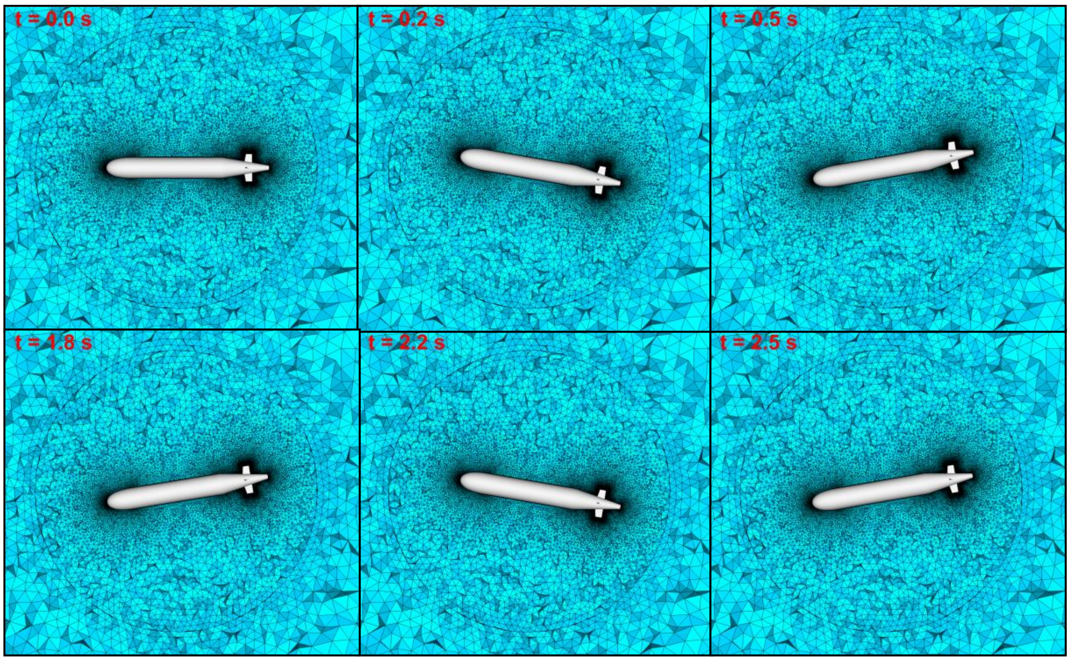

Figure 6.7 Change of Volume Grid With Respect to Time for Combined Motion Simulation

6.2.2 Boundary Conditions

Same boundary conditions with pure heave simulation are defined for domain boundaries. On the other hand sliding mesh cell zone condition is defined for inner domain and mesh motion is defined by using an UDF file. Interface BC is defined for the two faces that separate sub-domains, velocity inlet BC is defined for front and lower faces, pressure outlet BC is defined for back and upper faces and symmetry BC is defined for side faces. Flow domain and defined boundary conditions are illustrated in Figure 6.8:

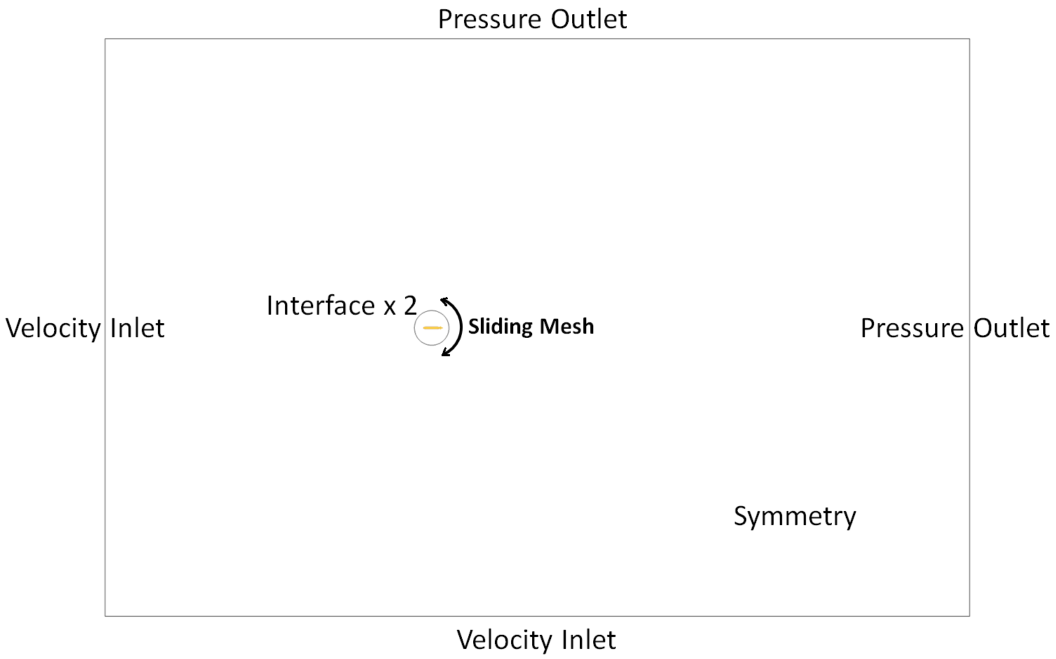

Figure 6.8 Flow Domain and Defined Boundary Conditions for Combined Motion Simulation

6.2.3 CFD Simulation Results

Combined motion is simulated for Autosub AUV model. Transient CFD analysis is performed for given cruise conditions in Table 6.3 and it is intended to obtain q and $\dot{q}$ dependent dynamic coefficients.

Table 6.3 Cruise Conditions for Combined Motion Simulation

Free-stream Velocity (m/s)	2.69
Amplitude (°)	10
Frequency (Hz)	1.5
Ambient Pressure (Pa)	150277

Same as the pure heave simulation, combined motion is defined with a sinusoidal function by using an UDF file. Same as the pure heave motion simulations, sinusoidal function defined by Equation (6.1).

Time dependent force and moment coefficients on the z direction are obtained from CFD simulation and results are compared with experimental data [13]. Results are given in Figure 6.9 and Figure 6.10:

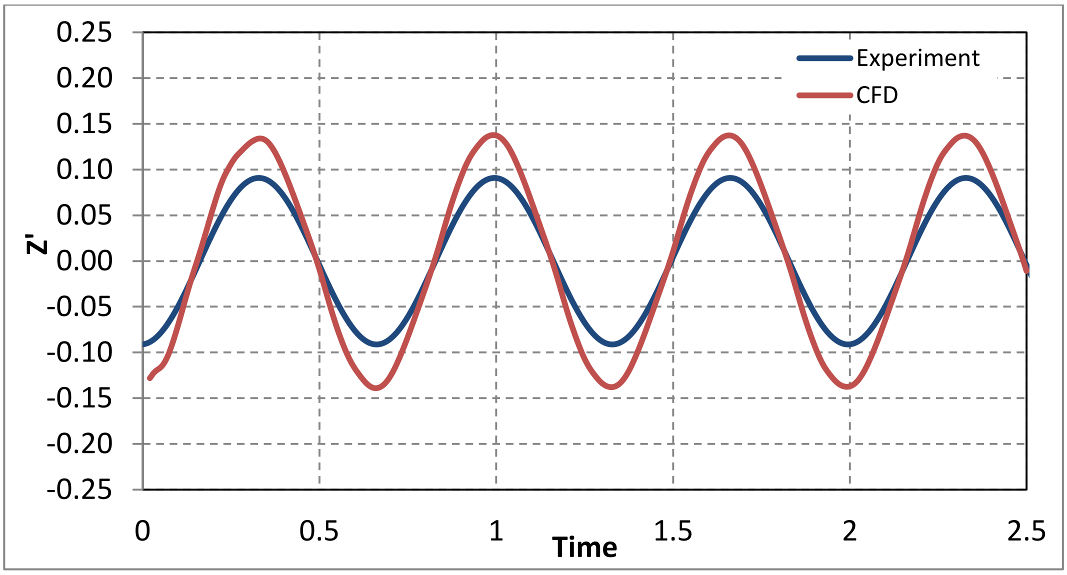

Figure 6.9 Z Force Coefficient With Respect to Time for Combined Motion Simulation [13]

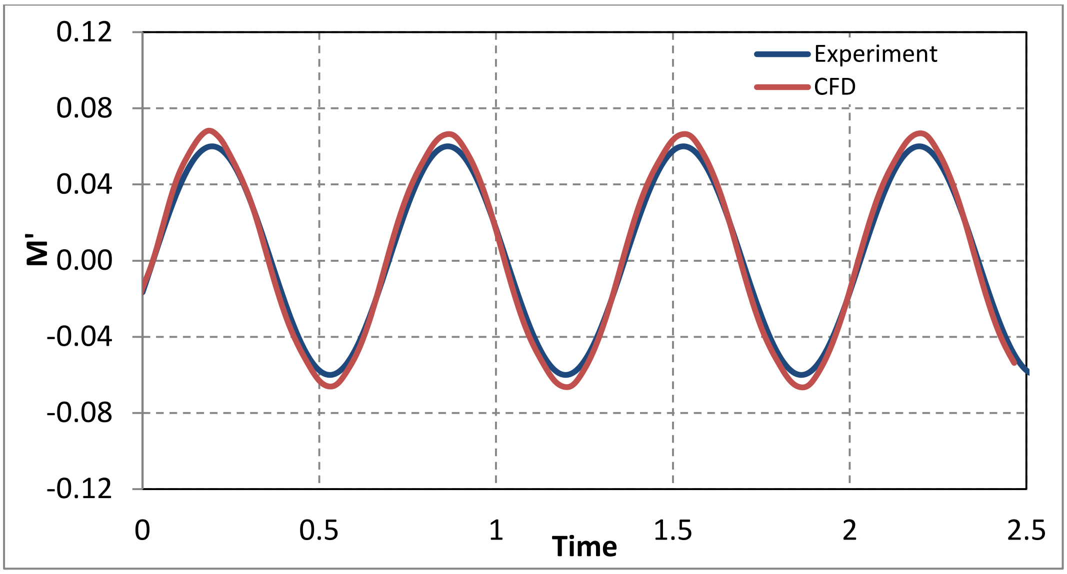

Figure 6.10 Pitch Moment Coefficient With Respect to Time for Combined Motion Simulation [13]

Equation (6.2) and Equation (6.3) are used to obtain experimental data in figures from given dynamic coefficients and combined motion includes all terms in these equations. Similar to the pure heave results, these equations are used for regression analyses to obtain q and $\dot{q}$ dependent dynamic coefficient from time dependent CFD results. Since w and $\dot{w}$ dependent coefficients are calculated from pure heave results, they are used as an input for combined motion regression analyses to simplify calculations. MINITAB commercial program is used for regression analyses and obtained dynamic coefficients and experimental data are given in Table 6.4:

Table 6.4 Calculated Dynamic Coefficients from Combined Simulation and Experimental Data

Coefficient	CFD (x10^3)	Experiment (x10^3)	Error (%)
Z'_q	-23.60	-11.22	110.0
M'_q	-5.34	-5.04	5.9
$Z'_{\dot{q}}$	-0.293	-0.169	73.4
$M'_{\dot{q}}$	-1.1	-0.98	12.2

As shown in Table 6.4, results of Z force derivatives have unacceptable error percentages for an AUV design process. This difference can be seen from Figure 6.9 too. On the other hand results of pitch moment derivatives are in good agreement with experimental data and maximum error is 12.2%. However force and moment results constitute an inconsistency that occurs because of the miscalculated location of center of pressure. Therefore results of combined motion simulation are not reliable. In conclusion, Z force results are not in good agreement with experimental data and pitch moment results are not reliable. Therefore using RA simulation methods to obtain of q and $\dot{q}$ dependent dynamic coefficients will be more appropriate than combined motion simulation method.

In addition similar to the previous transient CFD analyses, CFD analysis is initialized as a steady analysis and after convergence of steady run transient CFD analysis is continued on steady CFD analysis data file to make convergence easy. Time step is selected as 0.005 s and 30 sub-iterations are made for transient CFD analysis. Overall CPU time is 9.8 days.

Besides flow field is examined and velocity distribution with respect to time is shown in Figure 6.11:

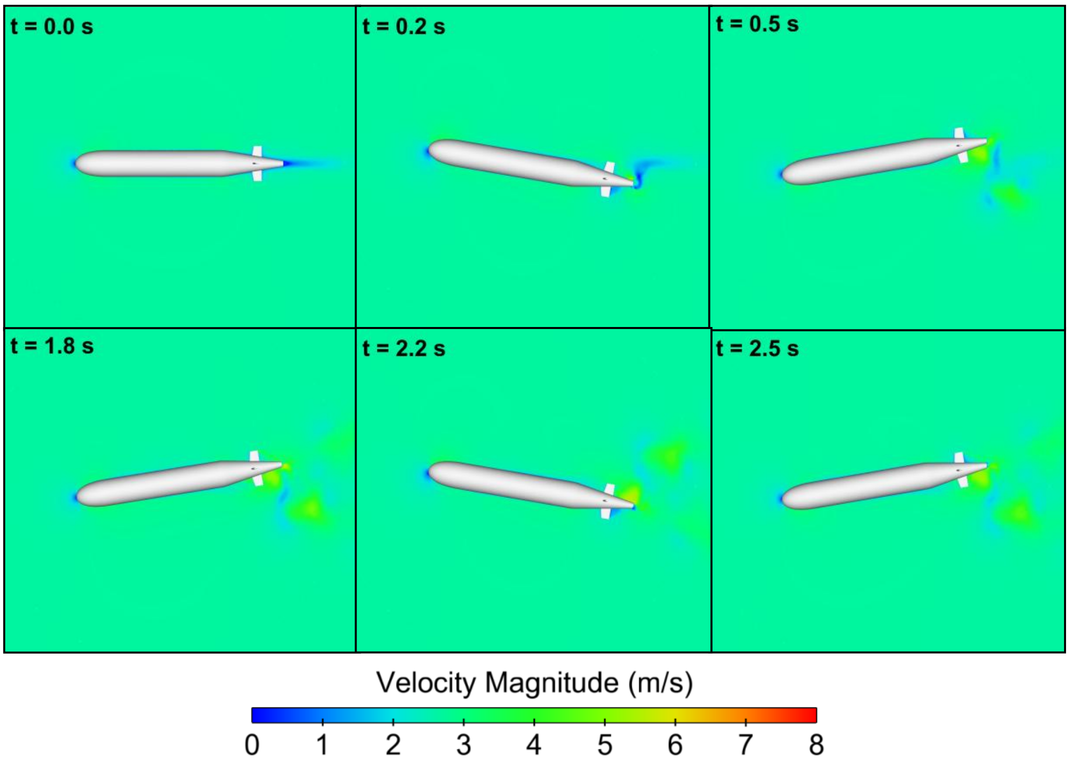

Figure 6.11 Velocity Distribution With Respect to Time for Combined Motion Simulation

CHAPTER 7

CONCLUSION AND FUTURE WORK

Prediction of hydrodynamic performance parameters is very important for an AUV design process. Conducting hydrodynamic tests is the most accurate way to do this prediction. However hydrodynamic tests are expensive applications and increase costs of hydrodynamic design projects. On the other hand CFD methods can be used as assistive tools for an AUV design processes with through the development of computer technology. In this way, number and costs of hydrodynamic tests can be reduced. In this study, CFD modelling techniques are composed to simulate hydrodynamic tests such as straight line towing, RA and PMM tests.

Autosub and DARPA SUBOFF test case models were used for CFD analyses. Before detailed CFD analyses, grid independence and turbulence model selection studies were performed to get accurate results in optimum time. First of all straight-line towing test was simulated for both of the models. Steady-state CFD analyses were performed for these simulations. After straight-line towing test simulations, static hydrodynamic coefficients were obtained for both of the test case models. Obtained coefficients were in very good agreement with experimental data.

The RA test was simulated for two different velocity profiles. According to first velocity profile RA test was simulated with constant angular velocity to obtain q dependent dynamic coefficients for Autosub model. Steady-state CFD analyses were performed for this simulation. Obtained dynamic coefficients were in very good agreement with experimental data and maximum error was below 10%. Then RA test was simulated for constant angular acceleration to obtain $\dot{q}$ dependent dynamic coefficients for Autosub model. Unsteady CFD analysis was performed for this simulation. Calculated dynamic coefficients were in good agreement with experimental data and maximum error was 16.6%.

PMM covers several motions which are given in Section 1.2.3.1. Pure heave and combined motion tests were simulated in this study. Unsteady CFD analyses were performed for both of the motion types. Pure heave motion was simulated to predict w and $\dot{w}$ dependent dynamic coefficients. Dynamic coefficients were predicted well but error percentages were higher than the previous results. It was indicated that complexity of motion could be the reason of this increment of errors. Then combined motion was simulated to predict q and $\dot{q}$ dependent dynamic coefficients. In addition results of pure heave motion simulation were used to calculate q and $\dot{q}$ dependent dynamic coefficients. Calculated moment coefficients were in good agreement with experimental data but calculated force coefficients were not consistent with experimental data. It was indicated force and moment results constitute an inconsistency that occurs because of the miscalculated location of center of pressure. Finally it was concluded that results of combined motion simulation were not reliable. Therefore using RA CFD simulations to predict q and $\dot{q}$ dependent dynamic coefficients would be more appropriate than using combined motion CFD simulations.

In the scope of future works, enhancing studies about combined motion CFD modelling is planned to get accurate results. Moreover pure pitch motion given in Section 1.2.3.1 can be simulated as an alternative CFD modeling method to predict q and $\dot{q}$ dependent dynamic coefficients.

REFERENCES

[1] T. W. Benanzer, System Design of Undersea Vehicles with Multiple Sources of Uncertainty, OH, USA: Wrigh State Univetsiy, 2008.

[2] A. Palmer, Analysis of Propulsion and Manoeuvring Characteristics of Survey-Style AUV and Development of a Multi-Purpose AUV, Southampton: University of Southampton, 2009.

[3] D. R. Blidberg, The Development of Autonomous Underwater Vehicles; A Brief Summary, Hampshire, UK: Autonomous Undersea Systems Institute, 2011.

[4] A. Philips, M. Furlong and S. Turnock, "The Use of Computational Fluid Dynamics to Determine Dynamic Stability of an Autonomous Underwater Vehicle," University of Southampton, Southampton, 2007.

[5] "The Towing Tank in the Center for Ocean Engineering at MIT," Massachuets Institute of Tecnology, [Online]. Available: http://web.mit.edu/towtank/www/facilities. [Accessed 14 May 2014].

[6] L. Ping, Hydrodynamic Coefficients of Maoeuvring For Small Vessels, Malaysia: Universiti Teknologi Malaysia, 2004.

[7] K. Rhee, H. Yoon, Y. Sung, S. Kim and J. Kang, "Experimental Study on Hydrodynamic Coefficients of Submerged Body Using Planar Motion Mechanism and Conning Motion Device," Seoul Nationa University, Korea, 2000.

[8] V. Bertram, Practical Ship Hydrodynamics, Duisburg, Germany: Butterworth Heinemann, 2000.

[9] Y. Ikeda, T. Katayama and H. Okumura, "Characteristics of Hydrodynamic Derivatives in Maneuvering Equations for Super High-Speed Planning Hulls," in *Tenth International Offshore and Polar Engineering Conference*, Seattle, USA, 2000.

[10] C. Williams, C. T.L., D. J.M., I. M.T. and A. F., "Effects of Hull Length on the Hyrodynamic Loads on a Slender Underwater during Manoeuvres," in *Oceans'06 MTS/IEEE Conference,* Boston, USA, 2006.

[11] L. David and C. Jackson, A Coning Motion Apparatus for Hydrodynamic Model Testing in a Non-Planar Cross-Flow, Massachusetts, USA: Massachusetts Institute of Techology, 1989.

[12] R. Roddy, "Investigation of The Stability and Control Characteristics od Several Configuration of The DARPA Suboff Model From Captive-Model Experiments," David Taylor Research Center, Bethesda, Maryland, 1990.

[13] N. Kimber and K. H. Scrimshaw, "Hydrodynamic Testing of A 3/4 Scale Autosub Model," Defence Research Agency, Hampshire, UK.

[14] J. Guo and F. Chiu, "Maneuverability of A Flat-Streamlined Underwater Vehicle," in *Robotics and Automation International Conference*, Taipei, Taiwan, 2001.

[15] D. Humphreys and W. K.W., "Prediction of Acceleration Hydrodynamic Coefficients for Underwater Vehicles From Geometric Parameters," Naval Coastal Systems Laboratory, Panama City, Florida, 1978.

[16] D. Jones, D. Clarke, I. Brayshaw, B. J.L. and A. B., "The Calculation of Hydrodynamic Coefficients for Underwater Vehicles," DSTO Platforms Sciences Laboratory, Victoria, Australia, 2002.

[17] E. d. Barros, A. Pascoal and E. d. Sa, Progress Towards a Method For Predicting AUV Derivatives, Sao Paulo, Brazil: University of Sao Paulo, 2008.

[18] A. Philips, M. Furlong and S. Turnock, "Virtual Planar Motion Mechanism Test of the Autonomous Underwater Vehicle Autosub," University of Southampton, Southampton.

[19] H. Zhang, Y. Xu and H. Cai, "Using CFD Software to Hydrodynamic Coefficients," *Journal of Marine Science and Application,* vol. 9, no. 2, pp. 149-155, 2010.

[20] S. Kim, B. Rhee and R. Miller, "Anatomy of Turbulent Flow around DARPA SUBOFF Body in a Turning Maneuver Using High-Fidelity TANS Computations," in *29th Syposium on Naval Hydrodynamics*, Gothenburg, Sweden, 2012.

[21] S. Arslan, Su Altı Araçları için Yeni Geliştirilen Hidrodinamik Modelleme Yöntemleri Kullanılarak Otonom Bir Su altı Aracının Hidrodinamik Karakteristiğinin İncelenmesi, Istanbul, Turkey: Istanbul Technical University, 2013.

[22] FLUENT 6.3 Documentation, 2006.

[23] Theory Guide, ANSYS FLUENT 12.0, 2009.

[24] G. Batchelor, An Introduction Fluid Dynamics, Cambridge,England: Cambridge Univ. Press, 1967.

[25] J. Hinze, Turbulence, New York, USA: McGraw-Hill Publishing Co., 1975.

[26] F. Menter, "Two-Equation Eddy-Viscosity Turbulence Models for Engineering Applications," *AIAA Journal,* vol. 32, no. 8, pp. 1598-1605, 1994.

[27] User's Guide, ANSYS FLUENT12.0, 2009.

[28] A. Chorin, "Numerical Solution of Navier-Stokes Equations," *Mathematics of Computation*, vol. 22, no. 104, pp. 745-762, 1968.

[29] G. Griffiths, P. Stevenson, A. Webb, N. Millard, S. McPhail, M. Pebody and J. Perrett, "Open Ocean Operational Experience with the Autosub-1 AUVs," Southampton Ocean Centre, Southapmton,UK.

[30] N. Millard, S. McPhaill, P. Stevenson, J. Perrett, A. Webb and G. Griffiths, "Remote Presence in the Marine Environment with the Autosub-1 AUV," Southampton Oceanography Centre, Southampton, UK.

[31] N. Kimber and W. Marshfield, "Design and Testing of a Control Surfaces for the Autosub Demonstrator Test Vehicle," Defence Research Agency, Haslar, 1993.

[32] N. Groves, H. T.T. and M. Chang, "Geometric Characteristics of DARPA SUBOFF Models," David Taylor Research Center, Bethesda, USA, 1989.

[33] K. Hoffman, Computational Fluid Dynamics Vol. 3, Wichita, USA: Engineering Education System, 2000.

[34] C. Brennen, "A Review of Added Mass and Fluid Inertial Forces," Naval Civil Engineering Laboratory, California, USA, 1982.